geosciences

MDPI

Article

Mantle-Derived Corundum-Bearing Felsic Dykes May Survive Only within the Lower (Refractory/Inert) Crust: Evidence from Zircon Geochemistry and Geochronology (Ivrea–Verbano Zone, Southern Alps, Italy)

Mattia Bonazzi [1,2,*], Antonio Langone [2,*], Simone Tumiati [3], Edoardo Dellarole [4], Maurizio Mazzucchelli [2,5], Tommaso Giovanardi [5] and Alberto Zanetti [2,*]

1 Dipartimento di Scienze della Terra e dell'Ambiente, Università di Pavia, Via Ferrata1, 27100 Pavia, Italy
2 Istituto di Geoscienze e Georisorse- C.N.R. U.O.S. of Pavia, Via Ferrata 1, 27100 Pavia, Italy
3 Dipartimento d Scienze della Terra, Università degli Studi di Milano, Via Mangiagalli 34, 20133 Milano, Italy; simone.tumiati@unimi.it
4 Sesia-Val Grande Global UNESCO Geopark, Corso Roma 33, 13019 Varallo (VC), Italy; presidente@sesiavalgrandegeopark.it
5 Dipartimento di Scienze Chimiche e Geologiche, Università degli Studi di Modena e Reggio Emilia, Via Campi 103, I-41125 Modena, Italy; maurizio.mazzucchelli@unimore.it (M.M.); tommaso.giovanardi@unimore.it (T.G.)
* Correspondence: mattia.bonazzi01@universitadipavia.it (M.B.); langone@crystal.unipv.it (A.L.); zanetti@crystal.unipv.it (A.Z.)

Received: 17 June 2020; Accepted: 18 July 2020; Published: 23 July 2020

Abstract: Corundum-rich (up to 55 vol.%) felsic dykes formed with albite, ±K-feldspar, ±hercynite and ±biotite-siderophyllite cut the lower crustal rocks exposed in the Ivrea–Verbano Zone (NW Italy). Zircon is an abundant accessory mineral and its investigation through laser ablation-inductively coupled plasma (multi-collector)-mass spectrometer (LA-ICP-(MC)MS) has allowed results to directly constrain the timing of emplacement, as well as petrology and geochemistry of parental melts. Zircons are characterized by very large concentration in rare earth elements (REE), Th, U, Nb and Ta, and negative Eu anomaly. U–Pb analysis points to Norian emplacement ages (223 ± 7 Ma and 224 ± 6 Ma), whereas large positive $\varepsilon Hf_{(t)}$ values (+13 on average) indicate a derivation from depleted to mildly enriched mantle source. The mantle signature and the corundum oversaturation were preserved thanks to limited crustal contamination of the host, high-temperature refractory granulites and mafic intrusives. According to the geochemical data and to the evidence of the development of violent explosions into the conduits, it is proposed that dykes segregated from peraluminous melts produced by exsolution processes affecting volatile-rich differentiates during alkaline magmatism. This work provides robust evidence about the transition of the geochemical affinity of Southern Alps magmatism from orogenic-like to anorogenic during Norian time, linked to a regional uprising of the asthenosphere and change of tectonic regime.

Keywords: LA-ICP-MS dating; zircon; felsic dykes; corundum megacryst; magmatic differentiation

1. Introduction

The petrogenesis of corundum (α-Al_2O_3) has been deeply investigated in the last decades either because corundum crystallization can provide valuable insights into the development of complex petrological processes [1] or for its importance in prospecting and mining gemstone deposits, e.g., [2].

Corundum may be formed under very different P-T conditions as a result of magmatic and metamorphic processes [3].

Experimentally determined liquidus phase relationships in the CaO-MgO-Al_2O_3-SiO_2 (CMAS) system indicate that at high pressure (2 GPa; [4]), the stability field of corundum is large, and it can be in equilibrium with quartz and sapphirine. Conversely, at lower pressure, typical of continental crust (1 GPa; [5]), corundum stability is restricted to high aluminous basalt compositions and at very high temperatures. Moreover, corundum cannot be directly in equilibrium with quartz, from which it is separated by the anorthite stability field, whereas the sapphirine stability field disappears. The segregation of magmatic corundum is essentially restricted to differentiated alkaline intrusives (syenite, monzonite) and rift-related alkaline volcanism. Conversely, the spectrum of the metamorphic processes and rocks involving the segregation of corundum is huge. It includes near-closed system, iso-chemical metamorphic reactions in silica-poor alumina-rich rocks and open-system, metasomatic introduction of fluids/melts in contact rocks leading fluids/melts and/or the host rock towards silica-poor alumina-rich composition. A special case of metamorphic segregation is represented by the anatexis of metapelites, during which silica enters the melt first, and corundum can crystallize in the aluminum-rich residue.

One of the main metasomatic reaction recognized leading to corundum segregation is the "Plumasite" type. "Plumasite" is the term attributed by Lawson [6] to felsic intrusives consisting of >16 vol.% grey or blue corundum in association with sodic plagioclase (typically oligoclase) and biotite, as documented in a pegmatitic dyke intruding serpentinized peridotite in the Plumas County, California. Successively, the term has been also attributed to rocks containing alkali feldspar and other accessory minerals. Plumasite-type metasomatic reaction involves the intrusion of granite pegmatites into ultramafic rocks, especially peridotites. This is accompanied by a "desilication" of the melts through precipitation at the melt-ultramafic rock interface of "blackwalls" made by tri-octahedral micas (siderophyllite and phlogopite-rich biotite). As a result, quartz is no longer stable in the melt, which becomes saturated in corundum. These rocks have been widely investigated since the beginning of last century in several parts of the world (Africa, Finland and Urals, Russia, China Alps, Greece; e.g., [7–11]). At the outcrop scale, plumasites occur as dykes, veins or small bodies.

An important feature of plumasite is the occurrence of large cm-sized corundum crystals, e.g., [6,12–14]. The occurrence of large corundum crystals attracted the attention of several authors especially at the beginning of the last century [6,12,13], but unfortunately corundum of plumasites are usually highly fractured and not of gem quality [2].

The Ivrea–Verbano Zone (IVZ; westernmost sector of the Southern Alps) records important examples of plumasites, e.g., [15] (see Figure 1a). In this area, corundum-rich felsic dykes were also recognized in different localities since Lelièvre [16]. The plumasite-type mineral assemblage is the most common among the corundum-bearing dykes, but other felsic rocks saturated in corundum were recognized (see Figure 1a,b). The historical "plumasite-dykes" crop out in the central and southern IVZ, where they do not intrude ultramafics, but instead intrude (i) gabbroic rocks belonging to the Upper-Carboniferous–Lower Permian Mafic Complex and (ii) granulite-facies rocks of the crystalline basement of the Adria Plate ([13,17–19].

A comprehensive investigation on these rocks is missing. More recently, a corundum-rich diorite swarm has been documented in gabbroic/dioritic gneiss (the External Gabbro unit) of the Finero Complex, in the northernmost tip of IVZ [14] (see Figure 1). Moreover, in the Finero Complex, both nepheline-bearing corundum-free [20,21] and corundum-bearing diorites [22] are emplaced between mantle peridotite (the Finero Phlogopite Peridotite unit; FPP) and crustal, deep magmatic units (the Layered Internal Zone and the Amphibole Peridotite).

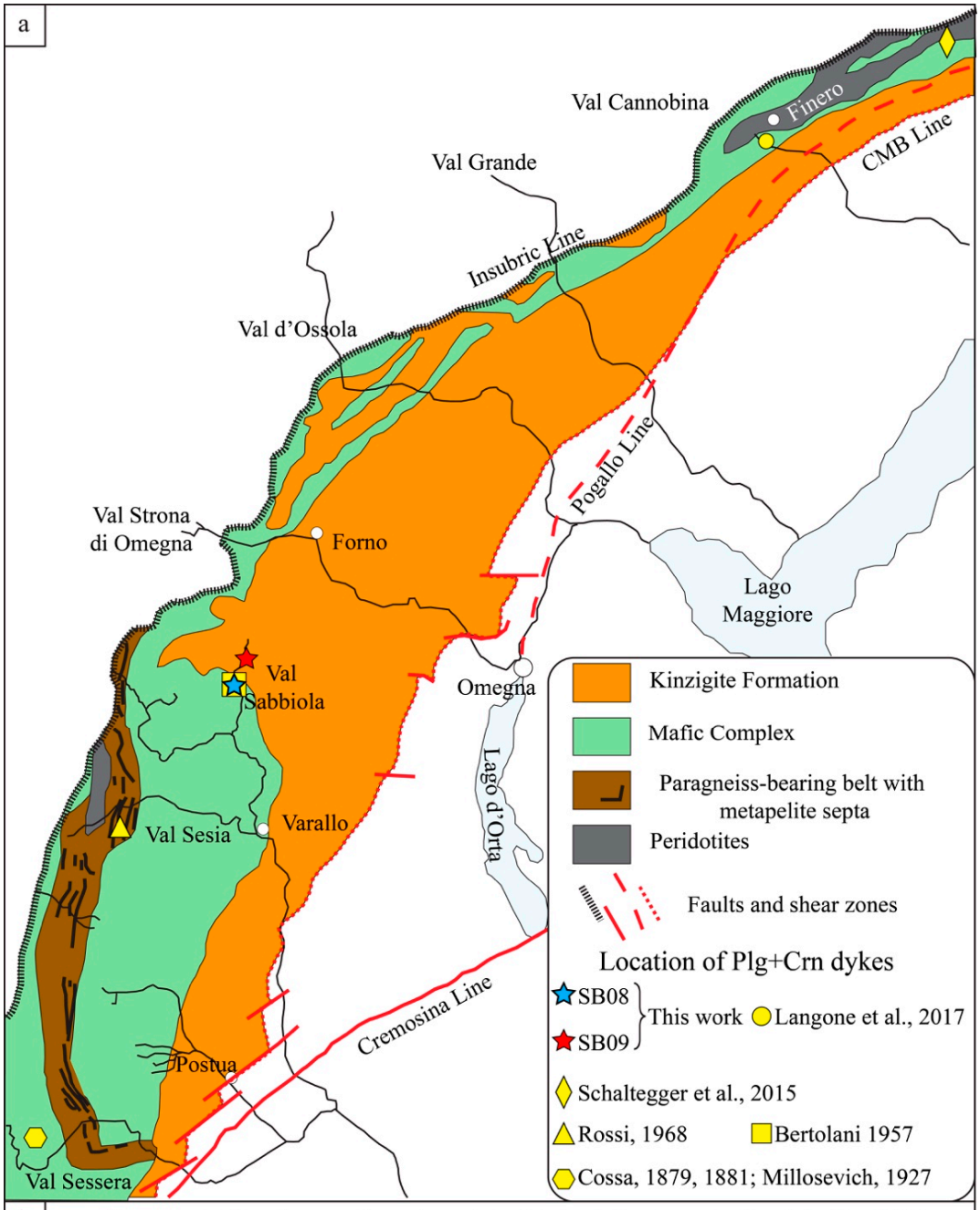

Minerals / References	Pl	Crn	Kfs	Bt	Ms	Grt	Sil	Czo	Hbl	Act	Chl	Nph	Ap	Qz	Sdl	Hc	Mag	Py	Opx	Ep
Cossa (1879) [17]	■	■	■																	
Millosevich (1927) [18]	■	■			+/-	+/-			+/-	+/-	■							+/-	+/-	+/-
Bertolani (1957) [13]	■	■	+/-		■		+/-		+/-		+/-			+/-						
Rossi (1968) [19]	■	■						■												
Schaltegger et al. (2015) [22]	■	■		+/-							+/-	■	■		+/-	+/-	+/-			
Langone et al. (2017) [14]	■	■	■										+/-			+/-	+/-			■
SB09	■	■	■	■												■	■			■
SB08	■	■		■												■	■			■

Figure 1. (**a**) geologic map of the Ivrea–Verbano Zone (modified after, Zingg [23] and Sinigoi [24]). The map shows the location of corundum-bearing dykes of the Ivrea–Verbano Zone (IVZ). (**b**) schematic table showing the mineral assemblages described for the felsic dykes in different samples and localities of the IVZ. Grey filled boxes indicate the common of local (+/-) occurrence of a mineral phase within the dyke. Abbreviations after Whitney and Evans [25].

A common feature of corundum-bearing felsic dykes is the occurrence of zircon as accessory mineral, locally with mm- [14] to cm-sized, e.g., [22] crystals. This mineral can incorporate and retain trace and rare earth elements (REE), including radioactive nuclides of U, Th, Lu and Hf, and it is commonly used in petrology to investigate igneous and/or metamorphic process, e.g., [26,27]. As far we are aware, there are no papers in literature reporting comprehensive geochemical investigations of zircon from corundum-saturated dykes. Thus, geochronological, geochemical and isotopic survey has been performed by laser ablation-inductively coupled plasma (multi-collector)-mass spectrometer (LA-ICP-(MC)-MS) on zircon grains from a couple of historical corundum-saturated felsic dykes of the central IVZ. This approach allowed us to determine the age of emplacement and place valuable insights on the origin of the parental melts and the petrologic processes leading to corundum oversaturation.

2. Materials and Methods

Felsic dykes are recognized in two localities of the Sabbiola Valley (lateral valley of Val Mastallone): (i) the SB08 dyke is located along the road to Montata village, near to the bridge of Salaro; (ii) the SB09 dyke is located at Alpe Campo (Figure 1a). These samples were studied in four thin sections (SB08, SB09A, SB09B and SB09C); zircon grains were studied directly in thin section and as separates. Zircon grains were separated following the traditional procedure: Grinding, hydrodynamic separation, magnetic separation by Frantz and density separation using heavy liquids (bromoform 2.84 g/cm^3 and diiodomethane 3.32 g/cm^3). Zircons as free as possible from fractures and inclusions were mounted in epoxy resin, polished and characterized for their internal structure by cathodoluminescence (CL) at the scanning electron microscope (SEM). The list of techniques adopted for each sample are reported in Table S1 and major elements based on electron micro probe analyzer (EMPA) analyses are reported in Table S2. The data collected on zircon grains for both samples are reported in the Supplementary Materials (from Tables S3–S7).

2.1. LA-ICP-MS U–Pb Dating and Trace Element Composition

Zircon U–Pb dating and trace element characterization with laser ablation ICP-MS were performed at the LA-ICP-MS laboratory of the CNR-IGG S.S. of Pavia. Trace element composition was determined by using a 213 nm Nd:YAG laser microprobe (NewWave Research) to a quadrupole ICP-MS system (DRCe from PerkinElmer). NIST-SRM610 was used as an external standard, whereas ^{29}Si was adopted as internal standard. In each analytical run the USGS reference sample BCR2 was analyzed together with the unknowns for quality control. Precision and accuracy are better than 5% and 10%, respectively. Trace element mineral compositions are reported in Tables S3 and S4.

In situ U–Pb geochronology was determined by using an ArF excimer laser microprobe at 193 nm (Geolas200Q-Microlas) with a sector field high-resolution ICP-MS Element I from ThermoFinnigan. The analytical method is basically that described by Tiepolo [28]. Instrumental and laser-induced U/Pb fractionations were corrected for using as external standard the GJ-1 zircon [29]. The same integration intervals and spot sizes were used on both the external standard and unknowns. During each analytical run reference zircon 91,500 [30] and Plešovice [31] were analyzed together with the unknowns for quality control (Supplementary Data Appendix 3). The spot size was set to 25 μm and laser fluency to 8 Jcm^{-2}. Data reduction was carried out using the "Glitter" software package [32], setting the error of the external standard at 1%. During each analytical run the reproducibility on the standards was propagated to all determinations according to the equation given by Horstwood [33]. After this operation, analyses are considered accurate within the quoted errors. Concordant ages were calculated using the Isoplot/EX 3.0 software [34]. All errors in the text are given at 2σ level.

2.2. Zircon Hf Isotopes

In situ Lu–Hf isotope analyses were determined at the laboratories of the "Centro Interdipartimentale Grandi Strumenti" of the University of Modena and Reggio Emilia (Italy). Analyses were carried out using a double focusing MC–ICP-MS with a forward Nier–Johnson

geometry (Thermo Fisher Scientific, Neptune™), coupled to a 213 nm Nd:YAG laser ablation system (New Wave Research™). Procedure is described in detail in [35].

Isotopic ratios were acquired in static mode with a block of 1000 cycles (including laser warm-up, ~100–160 cycles of analysis and washout), an integration time of 0.250 s, a laser spot of 55 µm and a fluence of ~10 J/cm^2. The laser frequency was ~10 Hz with a He flux of ~0.5 L/min. Before each analysis, the surface of the zircon was pre-ablated with a spot size of 60 µm. During the analytical session an in-house zircon reference materials MRD42-A was employed to check accuracy and precision of the measurements. A TEMORA 2 zircon reference material was analyzed at the beginning and at the end of the session.

Data reduction was performed with the Hf-INATOR excel spreadsheet [36]. TEMORA-2 yielded a $^{176}Hf/^{177}Hf$ ratio of 0.282700 ±0.000040 (2σ; n = 4, identical within error to the reference value of 0.282693; [37]) and MRD42-A yielded a $^{176}Hf/^{177}Hf$ ratio of 0.282158 ±0.000082 (2σ; n = 8; in-house standard MRD42-A of CIGS—Centro Interdipartimentale Grandi Strumenti of Modena and Reggio Emilia University; reference value: 0.282164).

Lu–Hf analyses were carried out on the same domain of U–Pb analyses and recalculated to the $^{206}Pb/^{238}U$ single spot age when possible. Otherwise, Lu–Hf data have been recalculated to 223 Ma, considering this age as the best representative for the complex intrusion age (see discussion). Data were calculated using the $(^{176}Lu/^{177}Hf)_{CHUR}$ present-day values of 0.282772 and 0.0332 respectively, as reported by Blichert-Toft and Albarède [38].

2.3. Thermodynamic Modelling

Thermodynamic modelling was performed with the software package Perple_X package (http://www.perplex.ethz.ch; [39]), the thermodynamic database of Holland and Powell [40] revised by the authors in 2002 (hp02ver.dat) and the solid solution models: Bio(TCC) for biotite, Mica(CF) for white mica, Gt(HP) for garnet, Cpx(HP) for clinopyroxene, Pl(I1,HP) + OrFsp(C1) + AbFsp(C1) for feldspars, Sp(HP) for spinel, St(HP) for staurolite and Amph(DHP) for amphibole.

3. Geological Setting and Geochronological Background

The IVZ represents an uplifted part of the pre–Alpine intermediate–lower continental crust located in the southern Alps of northwest Italy, e.g., [41]. It extends lengthwise for a distance of ~120 km and is bounded by two major fault zones, the Insubric Line in the northwest and the Cossato–Mergozzo–Brissago Line (CMBL) in the southeast (Figure 1a). The latter was active in the Permian (271 ± 1) and was reactivated also in more recent times ~147.3 ± 6.5 [42–44]. Locally, the CMB mylonites are crosscut and partially overprinted by mylonites of the Pogallo Line (PL; Figure 1a) which is interpreted as a low–angle normal fault due to crustal thinning [45], active during Early Mesozoic time (210–170 Ma; [46]).

The southern part of the IVZ (e.g., Val Sesia) has been traditionally subdivided in three main lithological units: Kinzigite Formation (supracrustal metamorphic rocks), Mafic Complex (intrusive mafic rocks; Figure 1a) and mantle peridotite. These units show a SW–NE strike and a broad metamorphic gradient increasing from amphibolite to granulite facies from SE towards NW e.g., [23,41,47,48]. The Kinzigite Formation occupies the south-eastern sector and originally was the upper part of the tilted crustal section (Figure 1a). It consists of siliciclastic metasediments with intercalation of metabasic rocks and minor calcsilicate rocks and marbles. The most studied outcrops of the Kinzigite Formation are exposed in Val Strona di Omegna (Figure 1a) where the metasedimentary rocks show a continuous metamorphic gradient from amphibolite– to granulite–facies conditions, e.g., [48]. The Kinzigite Formation structurally overlies the Mafic Complex (MC, Figure 1a) that was emplaced during Permian (from 292 to 282 Ma; e.g., [49]) and consists of gabbro, norite and diorite, e.g., [50].

U–Pb geochronological studies on zircon show that high-temperature (HT) metamorphism occurred during late Carboniferous to Permian (316–258 Ma) and that metamorphic events are not totally linked to intrusive events of the Mafic Complex, e.g., [51,52]. According to Klötzli et al. [53]

igneous pulses began intruding the deep and middle crust largely before (no later than 314 Ma) the emplacement of main magmatic system.

The magmatic pulse has been dated at ~292 to 282 Ma [49], nevertheless recently $^{206}Pb/^{238}U$ ages date the emplaced of main mafic complex in lower crust as ranging from 285.52 ± 0.15 to 281.58 ± 0.44 Ma [54].

After the main magmatic pulse, the lower crustal levels of the IVZ were intruded by several dykes, pegmatites and ultramafic pipes in a large time span from Permian to Jurassic, e.g., [14,53,55–59]. Garuti et al. [55] reported an intrusion age for the pipes coeval with the emplaced of mafic intrusives (Mafic Complex) at ~290 Ma ($^{207}Pb/^{206}Pb$ stepwise-evaporation method). Recent works suggest that ultramafic pipes formed during Triassic (249.1 ± 0.2 Ma); thermal ionization mass spectrometry (TIMS) U–Pb dating of zircon [56] (see Figure 2). These ultramafic/mafic bodies are associated to Ni-Cu-PGE sulfide mineralization derived from melting of metasomatized lithospheric mantle through the Variscan subduction and subsequently reactivated during the collapse of Variscan orogen [56,58]. Intrusion of small mafic bodies have been recently extended to Jurassic time by Denyszyn et al. [57]. These authors reported TIMS zircon ages at ~200 Ma from lower crustal pyroxenites and dunites that they interpreted as a distal and deep expression of the Central Atlantic Magmatic Province. A Jurassic age of emplacement (LA-ICP-MS concordant age of 187 ± 2.4 and 192 ± 2.4 Ma, see Figure 2) has been recently reported also for carbonatite bodies and dykes by Galli et al. [59] that they linked to sodic CO_2-bearing melts derived from an amphibole-rich mantle source. In particular, εHf values indicates a moderate crustal assimilation during emplacement of carbonatitic magma [59].

Towards the northern sector of the IVZ, i.e., the Finero area (Figure 2), the age of the main mafic magmatism is still poorly constrained showing evidences for emplacement at Carboniferous–Permian [14] and Triassic time [60]. In this sector the evolution of the lower crustal intrusives was associated to the development of several ductile shear zones established under HT conditions during Jurassic time [14,43] and almost pervasively overprinted the whole body. Furthermore, in this sector of the IVZ the lower crustal units are intruded by late pegmatitic leucocratic dykes and pods (Figure 1b), e.g., [14,20–22,61–63].

These bodies commonly contain abundant zircon grains subject of geochronological studies. Stähle et al. [20] obtained Triassic age (225 ± 13 Ma) from a Na-alkaline dioritic pegmatitic dyke using Pb/Pb evaporation technique. [64] dated zircon crystals from plagioclasite lenses by TIMS at 212.5 Ma (weighted $^{206}Pb/^{238}U$ mean age). Grieco et al. [62] reported other pegmatitic plagioclasite along the contact between peridotite and gabbro whose zircon grains provided U–Pb ages of 195 ±4 Ma and 202 ± 1 Ma (TIMS method). Schaltegger et al. [22] described nepheline-bearing syenite with zircon megacrystals (up to 9 cm). These authors dated pieces of large zircon grains using CA-ID-TIMS and obtained U–Pb data in the time range from 212 to 190 Ma. Recently Langone et al. [14] recognized some leucocratic dykes consisting of oligoclase, biotite, zircon, corundum and epidote within metagabbroic rocks. U–Pb dating of millimeter sized zircon grains suggested a wide time span from Late Permian to Early Jurassic.

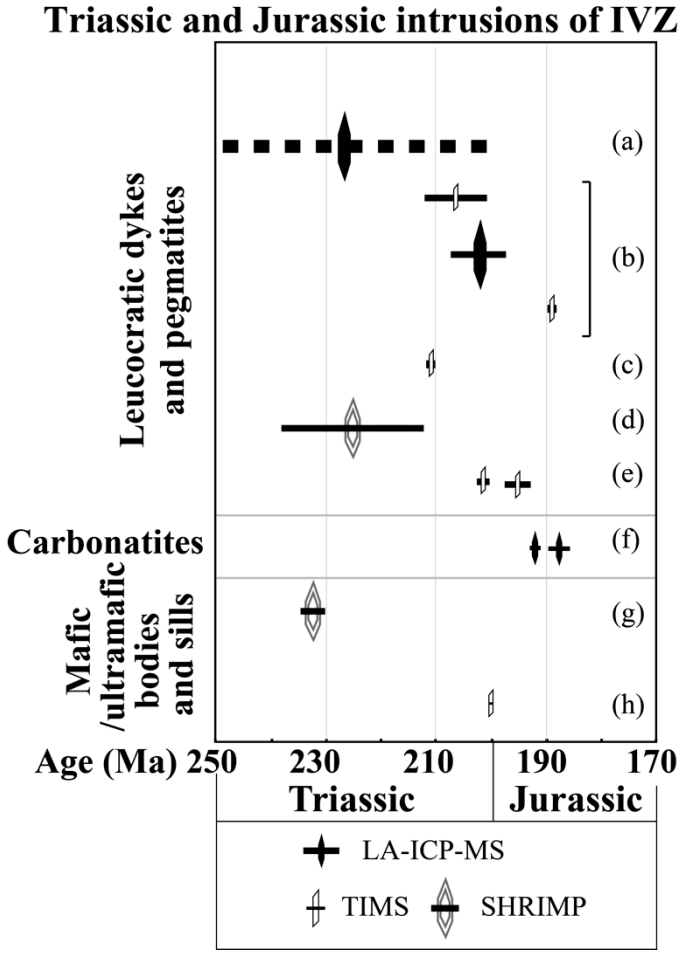

Figure 2. Schematic diagram showing U–Pb data from magmatic intrusions in the IVZ in the time span from Triassic to Jurassic. References: (**a**) [14]; (**b**) [22]; (**c**) [64]; (**d**) [20]; (**e**) [62]; (**f**) [59]; (**g**) [60]; (h) [57].

4. Results

4.1. Field Evidence, Petrography and Mineral Chemistry

The leucocratic dyke SB09 intrudes granulite-facies metasediments (locally called Stronalite) forming the metamorphic basement of the Adria plate. It has got a thickness up to 40 cm and shows sharp contacts with respect to the host rock. The intrusive rock is a (leuco)monzonite with hypidiomorphic granular texture (Figure 3a): It consists of corundum (~55 vol.%; 0.44–0.89 wt.% Fe_2O_3), albite (20 vol.%; An = 6–9%, Or = 0.6–2.1%), K-feldspar (20 vol.%; Ab = 9–24%), biotite (3–4 vol.%; molar Mg#, with Fe_{Tot} as Fe^{2+}, = 0.14–0.22, Al_2O_3 up to 21.9 wt.%; TiO_2 mostly in the range of 0.8–1.6 wt.%, with only one analysis of a small flake included in K-feldspar up to 3.5 wt.%) and hercynite (1–2 vol.%; Mg# = 0.04–0.05; 2.5–2.9 wt.% MnO; 0.5–0.9 wt.% ZnO). Corundum occurs as large (up to 1 cm) euhedral to subhedral crystals (Figure 3) and may include zircon, plagioclase and K-feldspar. It is common to observe corundum highly fractured and with polysynthetic twinning occurring parallel to the faces of the rhombohedron {1011}. Rarely, corundum shows lobate contours filled by albite and K-feldspar (Figure 3a). Backscattered electron (BSE) images revealed that K-feldspar has perthitic structure, containing exsolution lamellae of albite (Figure 3c): Thus, Na-richer analyses are likely to be more representative of the early alkali feldspar composition. Hercynite is always associated with biotite flakes: The size of the latter can vary from tens of microns to 5 mm. SEM observation revealed that hercynite is locally replaced by a fine-grained aggregate of corundum, Fe-gahnite (storing Zn) and magnetite (Figure 3f–g). Zircon is a common accessory mineral and generally occurs as clusters included within all rock-forming minerals (Figure 3c–e).

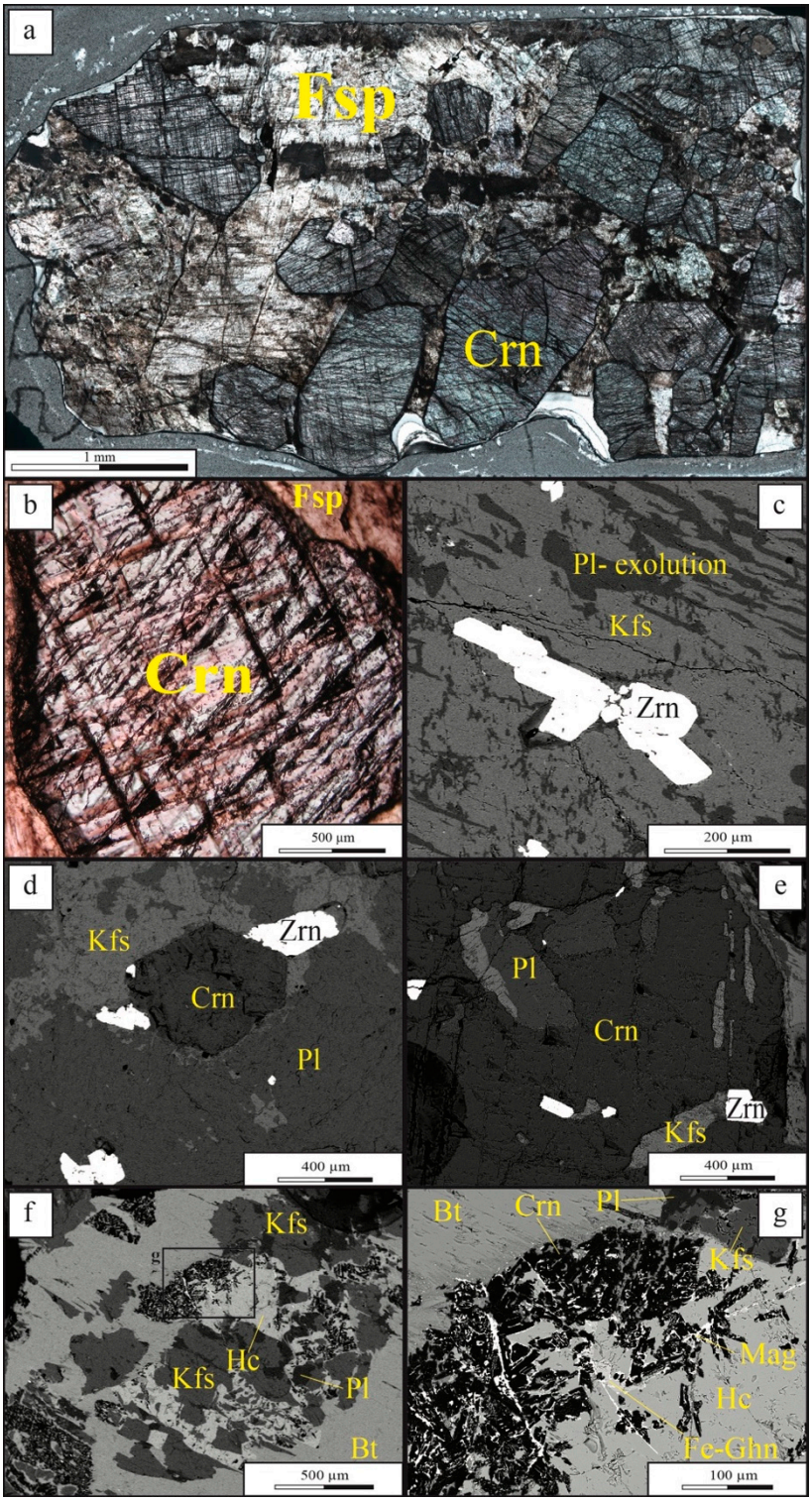

Figure 3. (**a**) Scan of SB09 thin section (80 µm thick) showing the magmatic/pegmatitic texture of the sample. (**b**) photograph of a euhedral crystal of corundum. (**c**) SEM-backscattered electron (BSE) image showing K-feldspar crystal with plagioclase exsolution and inclusions of zircon cluster. (**d**) SEM-BSE image of the mineral assemblage consisting of plagioclase, K-feldspar, corundum and zircon. (**e**) SEM-BSE image of zircons, K-feldspar and plagioclase inclusions within corundum. (**f**) SEM-BSE image of poikilitic biotite hosting spinels, K-feldspar and plagioclase. (**g**) detail of (**f**) showing reaction along the contact between biotite and hercynite consisting of corundum, magnetite and Fe-gahnite.

The leucocratic dyke SB08 intrudes an amphibole gabbro of the Upper Mafic Complex, reaching a thickness up to 50 cm. The studied dyke was localized and collected following the topographic map and the outcrop descriptions in Bertolani [13]. The dyke is made of several segments showing a zigzag configuration, e.g., [65]. The intrusive, leucocratic rock is a diorite, modally dominated by albite (~80 vol.%; An = 5–10%, Or = 0.4–1.7%) and with 20 vol.% corundum. In thin section, SB08 sample shows a porphyroclastic texture (blastomylonitic in Bertolani, [13]) with corundum and albite porphyroclasts surrounded by a fine-grained matrix consisting mainly of albite (Figure 4a,b). K-feldspar is absent. Corundum porphyroclasts are rounded or subehdral, usually highly fractured and with diffuse {1011} polysynthetic twinning: They are generally aggregated in clusters. Albite porphyroclasts show deformation bands, undulose extinction and deformation twinning. Zircon is the most abundant accessory minerals, whereas columbite and uraninite are rarer (Figure 4c). Biotite and oxides can be partially or totally replaced by fine-grain secondary minerals.

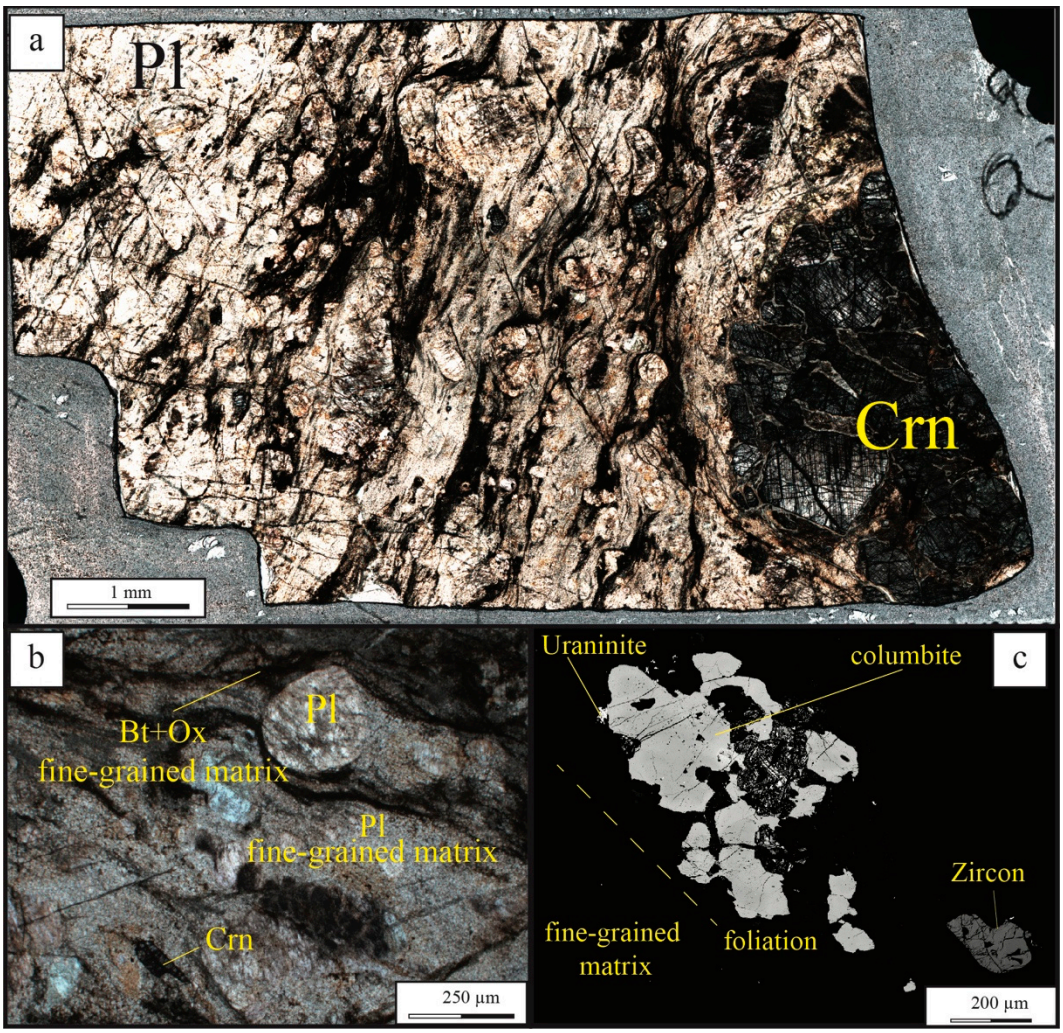

Figure 4. (**a**) scan of SB08 thin section (80 µm thick) showing the porphyroclastic texture. (**b**) microphotograph of plagioclase porphyroclasts embedded within the fine-grained matrix consisting mainly of plagioclase, oxide, biotite and corundum. (**c**) SEM-BSE image acquired with high contrast and low brightness showing columbite, zircon and uraninite within the fine-grained matrix.

The host rock of SB08 is an amphibole gabbro (SB06) consisting of labradoritic plagioclase (40 vol.%; An 54–68%), pargasitic amphibole (30 vol. %; 2–2.5 wt.% TiO_2; molar Mg#, with Fe_{Tot} as Fe^{2+}, 0.5; 13.5–14 wt.% Al_2O_3), altered pyroxene (15 vol.%), biotite (5 vol.%; 5–6 wt.% TiO_2; molar Mg#, with Fe_{Tot} as Fe^{2+}, 0.5–0.6; 15.2–16.2 wt.% Al_2O_3; annite/phlogopite). It shows granoblastic texture with

uniform grains size and generally straight, or occasionally smoothly curved, grain contact suggesting equilibration under granulitic facies condition without deformation-induced recrystallisation as observed in the SB08 leucocratic dyke.

EMPA analyses (Table S1) revealed that, in both, plagioclase does not show significant chemical variation neither from core to rim of large crystals nor among crystals in different textural positions (porphyroclasts vs. matrix) (Figure 5). The resulting albite composition differs from that reported for the typical plumasite, i.e., oligoclase. The latter usually characterizes the corundum-bearing leucocratic dikes of the IVZ (Figure 5). However, a corundum-rich leucocratic dyke with albite was already recognized by Bertolani [13], whereas a Ca-richer plagioclase (andesine) was found in a dyke intruding granulites in Val Sesia (Figure 5), [19]. The author suggested the name Dungannonite or Andesine-Plumasite for such andesine-bearing dyke.

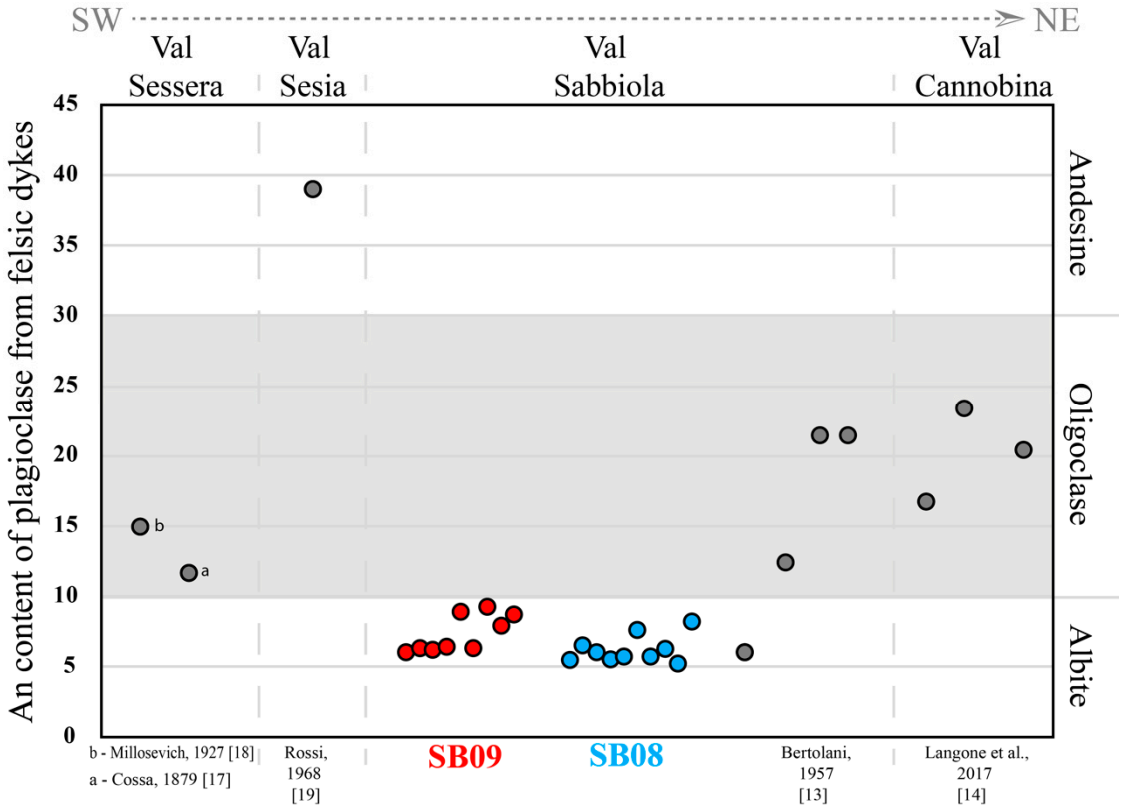

Figure 5. Anorthite content (An mol%) of plagioclase within corundum-bearing felsic dykes reported in different valleys of the of the IVZ, arranged from SW to NE. The red and blue circles show the composition of plagioclases for SB09 and SB08 dykes, respectively. The grey circles show the composition of plagioclases for other felsic dykes recognized in IVZ.

4.2. Zircon Internal Features

Zircon from both samples are characterized by complex internal features on CL-images (Figures 6 and 7): Oscillatory and sector zoning were observed within several grains as well as convoluted and/or homogeneous CL features.

Zircon grains in the hypidiomorphic granular dyke (SB09) are euhedral and subhedral, range in size from 50 to 200 μm. Generally, the grains show large cores with dark homogeneous CL features surrounded by thin brighter rims (Figure 6a). Completely homogeneous grains occur (Figure 6b,c), as well as zircon showing broad banding (Figure 6g) and sector zoning (Figure 6f–h). It is common to observe small inner cores with different zoning features with respect to the surrounding domains (e.g., Figure 6e,f). Some grains have domains characterized by patchy zoning (Figure 6e,j,k,l). Locally,

zircon grains are characterized by bright irregular CL features at the external domains or defining thin veins invading the inner portions (Figure 6c–i).

Zircon grains from the porphyroclastic dyke (SB08) show euhedral to subhedral shapes; the sizes range from 50 to 200 µm, as in SB09. Under CL the zircon grains show very complex internal features with inner domains characterized by different CL features with respect to the external domains (Figure 7b,c). Generally, the inner domains can be homogeneous or show oscillatory/broad band zoning, the latter ones can be locally faint (Figure 7g–k). Zircon domains showing convoluted zones are also frequent (e.g., Figure 7j–l) and more evident with respect to the SB09 sample. Bright irregular external domains are common and may propagate towards grain interior (Figure 7).

X-ray maps at the EMPA were performed on two zircon grains, one for each sample, and revealed that the zircons are characterized by tiny spots with high concentrations of U, Th and/or Y (Figure S2).

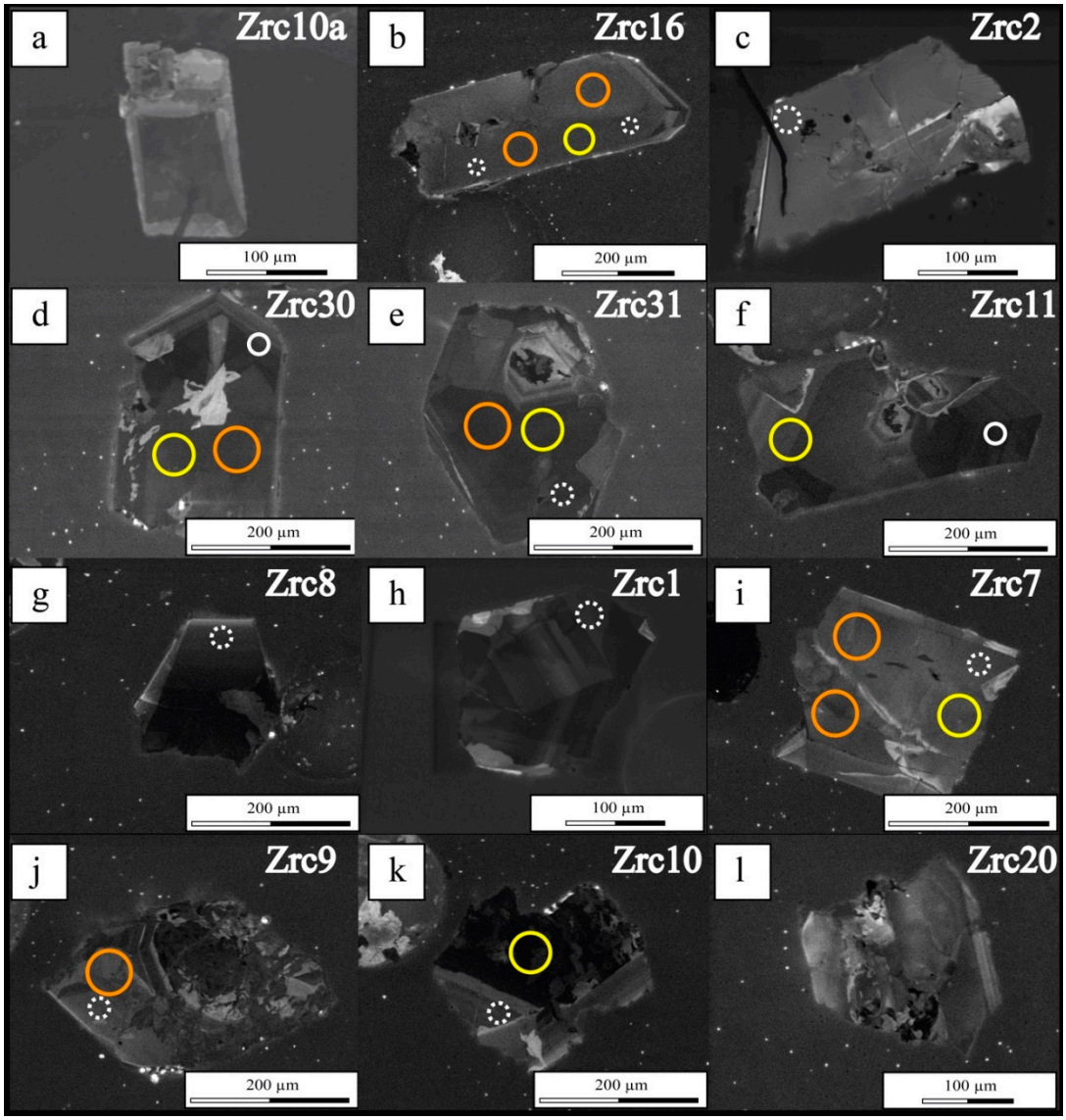

Figure 6. (**a**–**l**): SEM-CL image of zircon grains for sample SB09. The spot analyses are reported as circles: White dotted and solid circles refer to U–Pb concordant and discordant data, respectively; yellow and orange circles refer to trace element and Lu–Hf spot analyses.

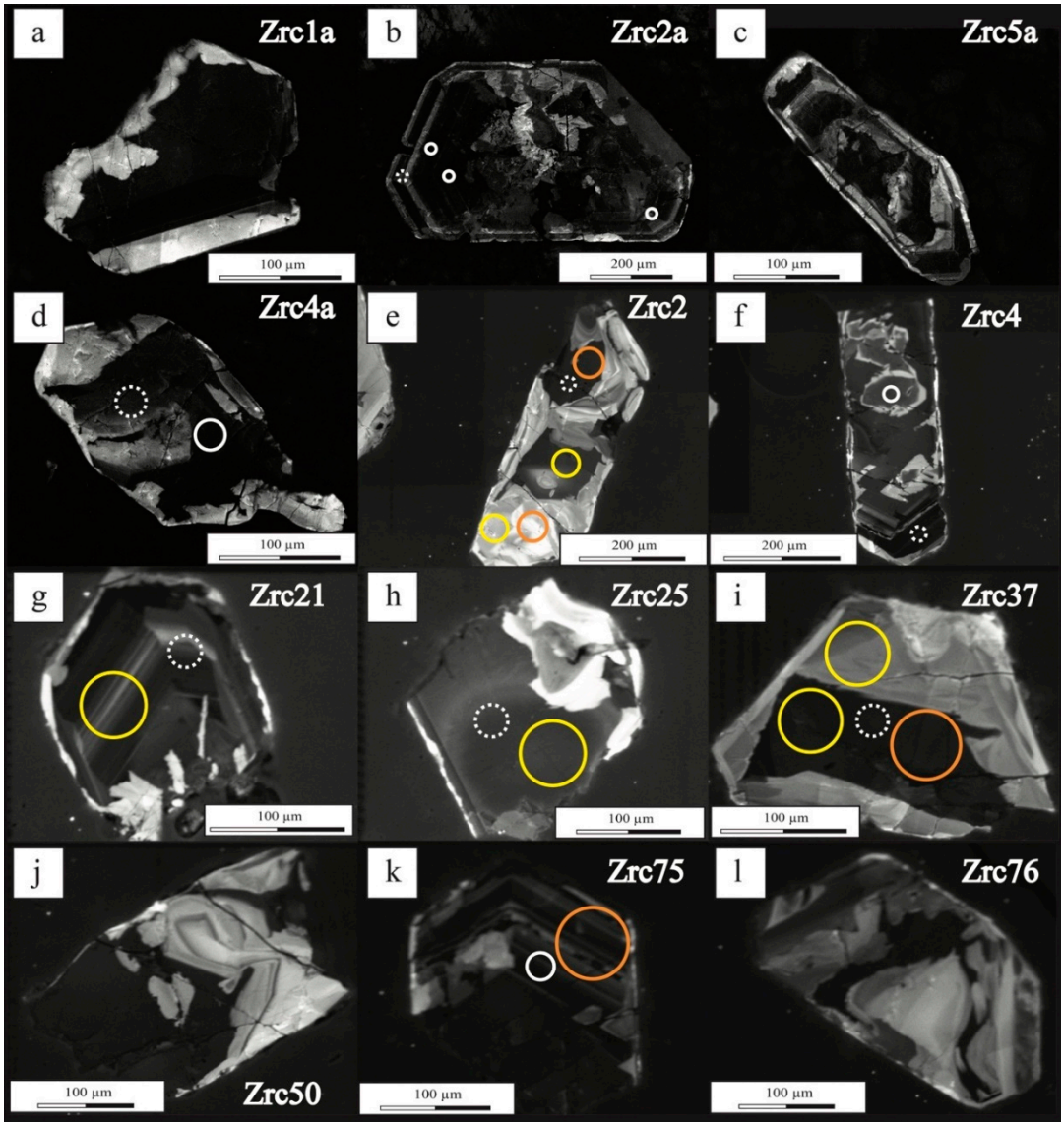

Figure 7. (**a**–**l**): SEM-cathodoluminescence (CL) image of zircon grains for sample SB08. The spot analyses are reported as circles: White dotted and solid circles refer to U–Pb concordant and discordant data, respectively; yellow and orange circles refer to trace element and Lu–Hf spot analyses.

4.3. Zircon Isotopic and Chemical Data

The U–Pb and Lu–Hf isotopic investigation has been targeted on homogenous domains and domains with oscillatory and sector zoning. Instead, all the domains, including those with bright or convoluted internal features, have been investigated to determine the trace element composition.

Forty-four U–Pb analyses (Figure 8a) were performed on 29 grains from SB09 dyke obtaining 14 concordant data with discordance <±2% in the range of 207 ± 6 to 227 ± 7 Ma (Figure 8b), with a weighted average age of selected eleven analyses at 223 ± 7 Ma (2σ error = mean of the errors). Fifty-one U–Pb analyses (Figure 8c) were performed on 32 grains for SB08 dyke; 23 isotopic ratios resulted concordant, with discordance <±2%, mainly in the range of 211 ± 5 to 236 ± 7 Ma, with a significantly older data at 247 ± 7 Ma (Figure 8d) and a weighted average age of selected fifteen analyses at 224 ± 6 Ma (2σ error = mean of the errors).

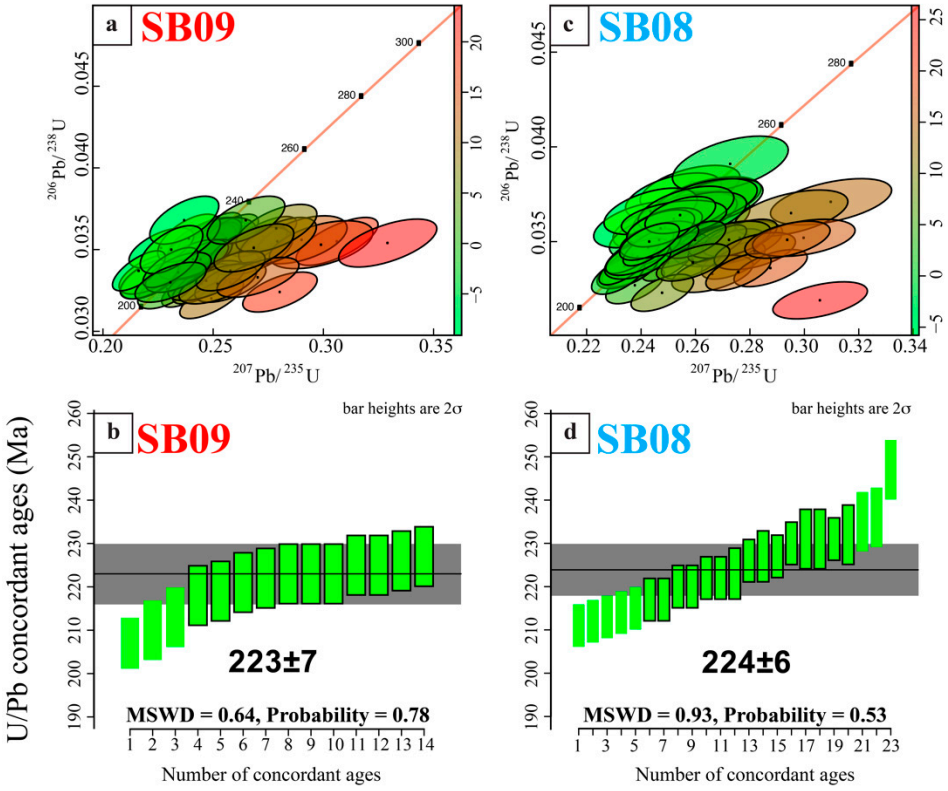

Figure 8. (**a**) and (**c**) U–Pb Concordia diagrams for SB09 and SB08, respectively. (**b**) and (**d**) diagrams of U–Pb concordant data for SB09 and SB08, respectively. The weighted average age reported on each diagram was obtained from data shown as green bars with black contours. Concordia diagrams and weighted mean plots have been performed using the IsoplotR toolbox [66].

Twenty-six trace elements analyses were performed on 23 grains for the SB09 dyke, whereas 27 trace elements analyses were performed on 17 grains for the SB08 dyke. The Hf content varies from 12,483 to 20,041 ppm and from 13,696 to 23,479 ppm for SB09 and SB08 samples, respectively. The total Hf content ranges without systematic variation as function of CL features. The total REE content is higher in zircons from SB09 (1575–4093 ppm) than in those from SB08 (402–2329 ppm). Both samples show exceptionally rich Th, U, Nb and Ta contents and similar REE patterns characterised by HREE enrichment over LREE (Figure 9a) with Eu and Ce defining negative and positive anomalies, respectively. Zircon grains from SB09 are characterized by a more pronounced negative Eu anomaly and higher M-HREE contents with respect to zircon grains from SB08. Generally, the concentrations of Y, REE, U, Th and Pb are higher in domains with dark homogeneous or oscillatory zoning than within zircon portions with bright and convoluted features at CL.

By comparing zircons from dykes studied in this work and from other Triassic–Jurassic intrusive bodies of IVZ it is evident that studied zircon grains are characterized by M-HREE contents significantly higher than those documented in zircons from leucocratic dykes, locally corundum-bearing, in the Finero Complex (northern IVZ; [14,22]) and carbonatites (central IVZ; [59]). The zircons in both felsic dykes are characterized by pronounced negative Eu anomalies that can be absent in the other local Mesozoic intrusions (Figure 9b). The REE patterns of zircon grains from the felsic dykes overlap the those reported for zircon grains hosted by large corundum xenocrysts in alkali basalts [67] (Figure 9c). A comparison with zircon REE patterns from different igneous rocks provided by Belusova et al. [68] and the studied zircon grains show REE patterns comparable with those reported for syenite-pegmatite, dolerite and granitoids for the HREE and match those from lamproite for LREE (Figure S3).

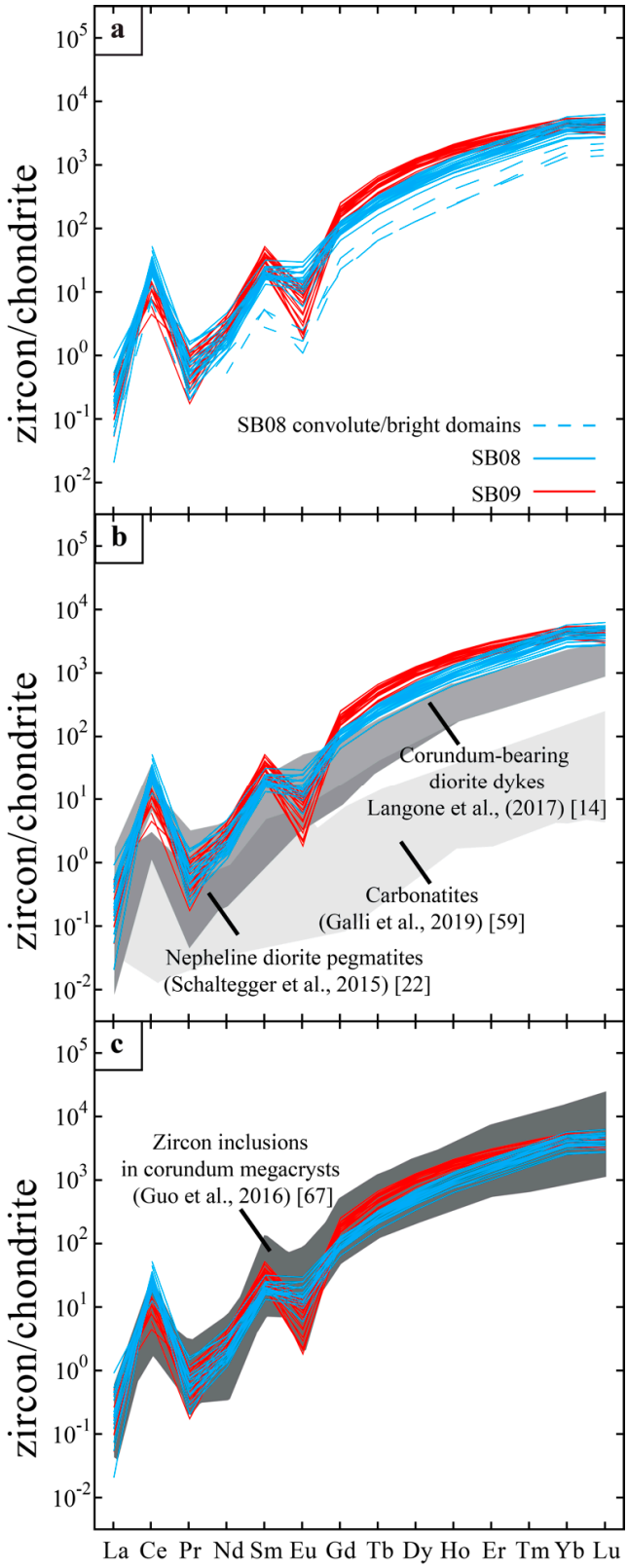

Figure 9. Carbonaceous Ivuna (CI) chondrite normalized rare earth elements (REE) patterns of zircon from SB09 and SB08 dykes (**a**), comparison with REE pattern of zircons of felsic dykes and carbonatites of the IVZ (**b**) and zircon included within corundum megacrysts in alkali basalts (**c**). CI normalization values are from McDonough and Sun [69].

Zircons from felsic dykes SB09 and SB08 show comparable isotopic Hf composition (Figure 10): In particular zircon grains from SB09 and SB08 show an average $\varepsilon Hf_{(t)}$ value of +11.7 (from +19.5 to +5.6) and +12.6 (from +17.6 to +8.8), respectively. Strongly positive $\varepsilon Hf_{(t)}$ values have been documented in zircons from leucocratic dykes, locally corundum-bearing, from the Finero Complex [14,22], whereas zircons from Central IVZ carbonatites and chromitites have negative $\varepsilon Hf_{(t)}$ values [59,70,71].

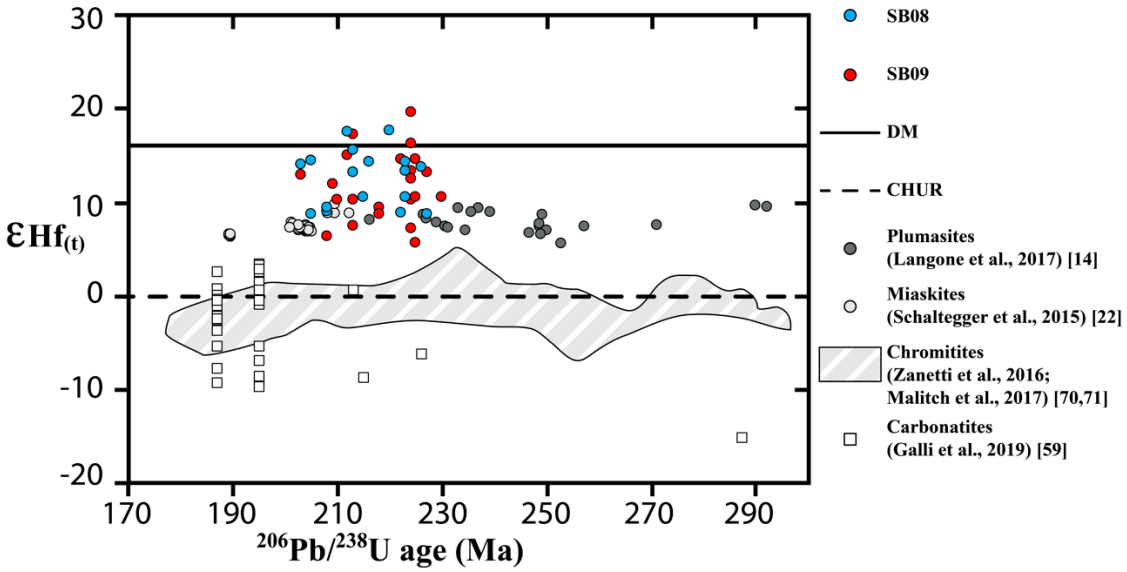

Figure 10. $\varepsilon Hf_{(t)}$ values from several magmatic bodies from IVZ. $\varepsilon Hf_{(t)}$ values are recalculated to the individual spot analysis $^{206}Pb/^{238}U$ ages.

4.4. Thermodynamic Modelling of Corundum-Bearing Felsic Dykes

Constraints on the P–T stability field of corundum-saturated mineral assemblages in the felsic dykes at sub-solidus conditions have been provided by means of thermodynamic modelling using the Perple_X package (http://www.perplex.ethz.ch; [39]), for thermodynamic database and the solution models that have been used see paragraph 2.3. P-T pseudosection (Figure 11) has been generated in the system Na_2O-K_2O-CaO-FeO-MgO-Al_2O_3-SiO_2 at water-saturated conditions for P ranging from 0.3 to 1.2 GPa and for T ranging from 650 to 950 °C for the bulk composition of the felsic dyke from Montata outcrop reported by Bertolani [13], which broadly corresponds to anorthosite sample SB08. This P-T range has been considered the possible conditions that IVZ was subjected from Permian to Triassic considering the P-T established by previous work, e.g., [72–74] (see paragraph 5.2 for details).

For the whole range of P-T conditions plagioclase is always stable, and its composition is low in anorthite (<10%), whereas corundum disappears at HP conditions. The mineral assemblage observed within anorthosite SB08 (corundum plus biotite plus hercynite plus plagioclase) is stable in a temperature range from ~700 to 950 °C for the considered pressure interval (0.3–1.2 GPa). Thermodynamic modelling predicts that nepheline is stable at higher temperature whereas garnet or sillimanite appear toward lower temperature conditions.

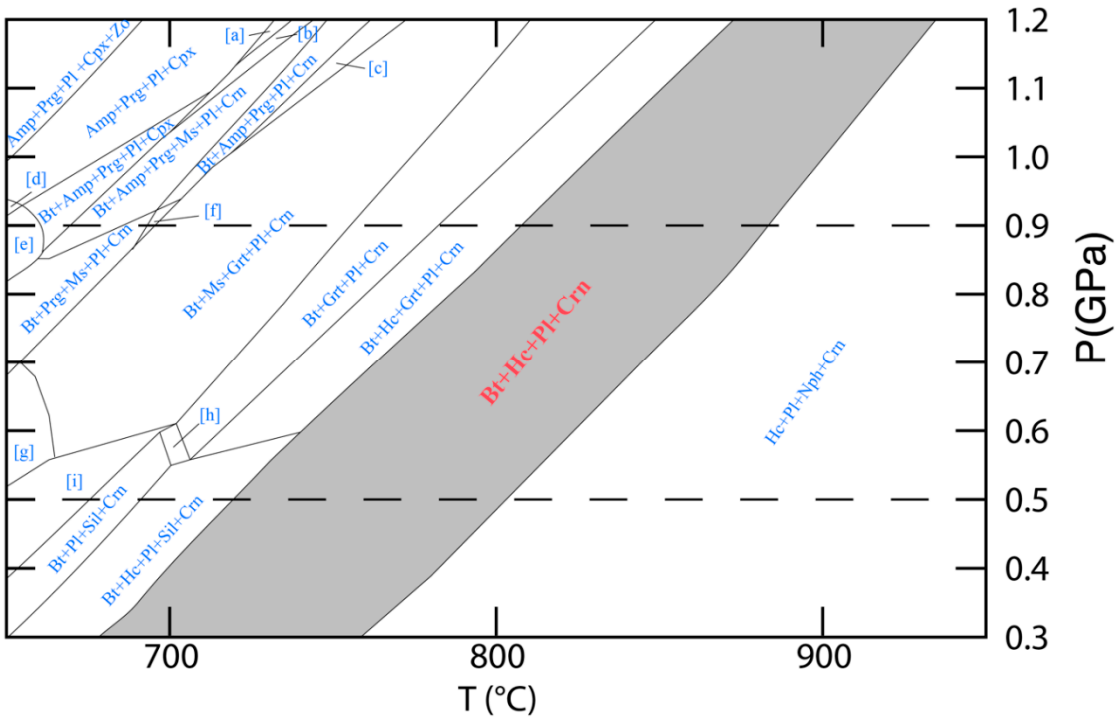

Figure 11. P-T pseudosection calculated for the chemical composition provided by Bertolani [13] for the plumasitic dyke recognized in Val Sabbiola, along the road to Montata village, which location and mineral assemblage correspond to our anorthosite SB08. The grey field corresponds to the mineral assemblage of SB08 rock. The dashed line indicates the pressure conditions estimated for the emplacement of the Mafic Complex during Carboniferous–Permian interval [72]. In the small stability field we reported the letters to indicate the mineral assemblage in those fields: [a]: Amp+Prg+Pl+Cpx+Crn; [b]: Bt+Amp+Prg+Pl+Cpx+Crn; [c]: Bt+Amp+Ms+Grt+Pl+Crn; [d]: Amp+Prg+Ms+Pl+Cpx; [e]: Bt+Amp+ Prg+Ms+Pl+Cpx; [f]: Bt+Ms+Pl+Crn; [g]: Bt+St+Ms+Pl+Crn; [h]: Bt+Gt+Pl+Sil+Crn; [i]: Bt+Ms+Pl+Sill+Crn. Abbreviations after Whitney and Evans [25].

5. Discussion

5.1. Field and Textural Constraints on Magmatic Process

In both felsic dykes, the occurrence of albite, zircon ±K-feldspar as inclusions within large corundum grains suggest they belong to the same mineral assemblage, that has been found worldwide in magmatic corundum from both alkali-rich intrusives and volcanic rocks, e.g., [2,75–77]. Although the studied rocks share almost the same mineral assemblage they are characterized by markedly different textures. Leucomonzonite SB09 shows a pegmatitic texture suggesting undisturbed crystallization of minerals from the melt.

The presence of large corundum and albite grains indicates that, also, the anorthosite SB08 was characterized by a pegmatitic texture overprinted by a later intense grain size reduction resulting in a porphyroclastic texture. It is interesting to note that the fine-grained, mylonitic fabric was already reported for the corundum-bearing felsic dykes from IVZ, e.g., [7,13,19,22]. Several lines of evidence indicate that the grain size reduction was imparted by a late magmatic process and not by shearing: (i) there is no evidence of shearing at both local and outcrop scales and (ii) the contacts between felsic dyke and the host gabbro have a magmatic zigzag configuration.

A penetrative syn-to-post crystallization deformation in Norian–Pliensbachian leucodiorite dykes (for a correct classification of these rocks see Mazzucchelli [78] intruding the mantle unit and the deepest crustal cumulates in the Finero Complex has already been documented [20–22]. Schaltegger et al. [22] report the development of breccia-like structure due to an "explosive" exsolution

of a volatile and LILE/HFSE-rich residual melt during late stages of crystallization at pressure corresponding to the mantle-lower crust transition. The exsolution of volatiles in nepheline syenite system has been considered responsible for violent "mantle explosions," being related to formation of peralkaline rocks, e.g., [79]. Similar "explosive" features have been recognized at mantle depths in intrusive rocks (mica-amphibole-rutile-ilmenite-diopside (MARID)) attributed to both lamproitic [80] and kimberlitic [81,82] melts. Explosions in phonolite systems were also recognized by Price [83]. Consistently, it is proposed that in the studied dyke (i.e., anorthosite SB08) an explosive release of volatiles from residual melts locally occurred and promoted very intense hydrodynamic fracturing and grain size reduction.

5.2. Timing and P-T Estimates for Felsic Dykes Intrusion

Euhedral zircon grains were found both as inclusions within large corundum, feldspar and biotite grains and along the grain boundaries together with the other rock-forming minerals. The exceptionally high concentration levels of Nb, Ta and U within zircons in both samples, suggest that the parental melts were enriched in these elements. Such enrichment is also supported by the crystallization of Nb, Ta, U minerals, which are also present as inclusions into zircon crystals (Figure S2). The concomitant strong Th enrichment shown by zircon also suggests the possible saturation in thorite of the melt. The large Al_2O_3 content of biotite-siderophyllite (up to 22 wt.%; Figure S1) and hercynite (60 wt.%) is further evidence of the peraluminous character of the parental melt and support their equilibrium with corundum. In this framework, zircon grains from the felsic dykes provide robust geochronological constraints on the magmatic evolution. Zircon crystals show very complex internal structures, frequently characterized by recrystallized domains and/or chaotic textures (see Figures 6 and 7). In both samples, the zircon grains have bright irregular domains replacing areas with magmatic textures (i.e., dark homogeneous, oscillatory and sector zoning). This process is interpreted as the results of late stage interactions of the zircons with fluids during cooling, e.g., [84–86]. The recrystallized zircon bright domains are lower in U, Th, Pb, Y, Nb and REE than the pristine zoned magmatic domains. This may suggest that recrystallization promoted migration of some incompatible elements [60,87]. For both samples, the obtained weighted average of the U–Pb concordant data (223–224 Ma; Norian) is interpreted as the crystallization age (Figure 8). Younger concordant ages are interpreted as the result of the perturbation of U/Pb system during late magmatic stages or at subsolidus conditions. The older concordant data are here interpreted as related to xenocrystic portions locally recognized under CL in some grains. The observation that the extent of the recrystallized domains is definitely larger in SB08 zircons, suggests a relationship with the late deformation stage related to volatile-driven overpressure and exsolution.

Considering the crustal level of emplacement of the felsic dykes studied here and the pressure gradients established during Upper-Carboniferous to Lower Permian times estimated along the Mafic Complex intrusives of Val Sesia [72] and the metamorphic rocks of Val Strona d'Omegna [73,74] a maximum intrusion P of ~0.7–0.6 GPa can be estimated. Taking into account a possible thinning of the continental crust between 2 and 4 km occurred during Lower Permian to Upper Triassic [48,88,89], a pressure range of 0.6–0.5 GPa (15–18 km depth) is considered as reliable estimate for the intrusion conditions of the felsic dykes during Norian time.

According to thermodynamic modelling (Figure 11) the observed mineral assemblage for SB08 dyke is stable at temperatures between 720–800 °C and 740–820 °C for 0.5 and 0.6 GPa, respectively. These P-T conditions can be considered to bracket the end of the crystallization and subsolidus equilibration. The temperature estimates are within the 685–900 °C range of the minimum temperature obtained for corundum crystallization from alkali melts by petrological investigations [90,91]. They are also strictly consistent with the 725–880 °C temperature interval determined for the onset of corundum crystallization from silicic melts at crustal to upper mantle conditions (0.6–1.1 GPa) through MELTS simulation by Sutherland et al. [76].

As far as we are aware, these are the most robust indirect constraints provided about the pressure conditions of corundum stability in natural melts. Our observations support the conclusions of Guo et al. [92], who suggest residence of magmatic corundum in alkali basalts at mid-crustal depths (0.5 GPa), while Sutherland et al. [76] argue a pressure between 0.5 and 1.0 GPa (15–30 km depth) for crystallization of magmatic corundum in felsic melts. Evidence for saturation of corundum at mantle depths is given by the peculiar association of corundum-bearing felsic assemblages with mantle peridotite xenoliths in the Scottish basalt province [93]. Summarizing, the occurrence of corundum-bearing felsic assemblages has been documented for pressure conditions from middle/lower crust to upper mantle.

5.3. A Possible Genetic Model of Corundum-Saturated Felsic Melts

The petrochemical features of the felsic dykes studied here provide a unique opportunity to place valuable constraints on the petrogenesis of corundum-oversaturated mantle melts. The possibility that some corundum was inherited from the host rocks is very remote, because it is a pretty rare and small accessory mineral in the host rocks of the felsic dykes, namely granulite-facies rocks of the metamorphic basement and the intrusive rocks of the Permian Mafic Complex [19,94]. Moreover, it is expected that corundum in disequilibrium with the host melt have anhedral crystal shapes, rounded edges and thick coronitic textures made by spinel, as found in corundum xenocrysts in alkaline basalts (e.g., [77] and references therein). In this frame, the local evidence of surface corrosion shown by few crystals from leucomonzonite SB09 does not necessarily indicate a xenocrystic origin, as this feature is also observed in basaltic phenocrysts due to reaction relationships resulting from changing temperature (and pressure) and/or local variation of melt composition during crystallization, e.g., [76].

The segregation of corundum, and the very large Al_2O_3 content of biotite-siderophyllite (22 wt.%) and hercynite (60 wt.%) in SB09 leucomonzonite, evidence a clear peraluminous character of the parent melts of the felsic dykes. The composition of hercynite and biotite-siderophyllite also indicates that the melts had very low Mg# value and Ti content, and high Mn and Zn values. The low modal content of mafic minerals and the plagioclase composition close to the albite end-member point to a very low overall concentration in Fe and Ca. According to the trace element zircon composition and to the occurrence of Nb-Ta-oxides and uraninite, it is concluded that the melts had exceptionally high concentrations in U, Th, Nb, Ta and REE (Figure 9, Figure S3). Thus, all the major and trace element composition converge in indicating that the melts were extremely evolved differentiates. This is also supported by (i) the estimated low-temperatures of end-crystallization/subsolidus equilibration, as down as 840–820 °C and (ii) the observations that the mineral assemblage consisting of albite-oligoclase, biotite-siderophyllite, K-feldspar, hercynite, zircon, columbite and uraninite is typically associated to magmatic corundum from strongly-evolved intrusives (nepheline-bearing and nepheline-free) syenite/monzonite in composition [2,15,95], and their corresponding volcanics (phonolites/trachytes), which are common in rift-related alkaline volcanism [2,76,77,89,90].

The strict similarity in U–Pb ages and isotopic Lu–Hf zircon composition, as well as in trace element zircon concentration and fractionation, suggests that the two felsic dykes studied here represent different steps of a differentiation process affecting a unique magmatic pulse. In this frame, the increase of M-HREE, Th, U, Nb and Ta and negative Eu anomaly in zircon (Figure 9a), and the appearance of K-feldspar in addition to albite suggest that leucomonzonite SB09 can be the more evolved differentiated produced by fractional crystallization dominated by feldspar precipitation. The larger amount of corundum in the SB09 leucomonzonite highlights a concomitant increase of the peraluminous character of the melt. Such a differentiation trend points forward to a syenite end-product, which is the most common corundum-bearing intrusive rock world-wide, e.g., [15,91,96,97]. A liquid line of descent involving the precipitation of diorite-monzonite-syenite sequence is typical of both silica-saturated to silica-undersaturated alkali-rich melts. However, there is an overwhelming evidence of the correlation of corundum-oversaturation during alkaline volcanisms, which has led to consider corundum saturation as the result of differentiation of mantle-derived alkaline basalts [15,90,91,98,99]. Nevertheless, available experimental investigations ([4,5]) do not show evidence for the existence

of a liquid-line-of-descent allowing for saturation in corundum starting from basalt composition, e.g., [77,92]. This has led to envisage a number of alternative petrologic scenarios.

In particular, Sutherland et al. [76] demonstrated by MELTS thermodynamic simulation that partial melting at shallow upper mantle conditions (1.1 GPa) of hornblende-bearing garnet/spinel pyroxenites and hornblendites may generate through fractional crystallization at P from 1.1 (mantle) to 0.6 (mid-crust) GPa residual liquids silicic, aluminous, alkaline and volatile-rich, with relatively low total FeO, CaO, MgO, TiO_2 and P_2O_5, capable of producing corundum-saturated leucocratic rocks. This scenario is supported by the results of MELTS simulation of the partial melting of phlogopite-amphibole-rich harzburgite forming the Finero Phlogopite Peridotite [100], which evidenced as the eutectic melts were silicic and corundum-normative. Nevertheless, this scenario appears of limited geological relevance, because mantle melts are commonly produced at definitely higher depths and are basaltic in compositions ([101] and references therein). The occurrence of nepheline in corundum-bearing intrusives e.g., [2,22] supports a genetic linking with silica-undersaturated melts.

In this regard, a number of hypotheses involving carbonate-components have been envisaged to explain the igneous crystallization of corundum, among which: (i) corundum crystallization from carbonatitic melts exsolved from differentiated alkaline melts (phonolites) derived from partial melting of spinel-facies amphibole-phlogopite-bearing carbonated lithospheric mantle [77]; (ii) corundum stabilization by interaction of a highly evolved, syenite/granite silicate melt with a carbonatitic melt at crustal levels [92]; (iii) differentiation of Fe-rich syenitic melts rich in CO_2 and H_2O, with formation of alkali-carbonate complexes and consequent oversaturation in [102].

Evidence of violent, explosive exsolution of volatile-rich melts is actually recorded in the anorthosite SB08, as well as in the Norian-Pleisbachian nepheline-bearing alkaline dykes of the Finero Complex [20–22]. Even though carbonates have been observed within Norian alkaline dykes [20,21], as well as in bands of the host mantle peridotites showing Norian metasomatic recrystallisation [103,104], they are absent within the studied felsic dykes suggesting that CO_2 was not a major component of the volatiles budget. This let us to suggest that the involvement of a carbonate component alone cannot justify the origin of corundum-bearing felsic dykes.

However, the widespread explosive characters of these leucocratic intrusions, locally saturated in corundum, suggest that exsolution may play a key role in producing those melts. Several schemes of melt-melt-fluid exsolution can take place in volatile-rich differentiated melts, e.g., [105–107]. In particular, exsolution of peraluminous silicate melts has been documented in evolved magmatic systems, having peralkaline silicate melts as complementary exsolved components [105]. Thus, we proposed a petrogenetic model in the frame of which corundum-oversaturation originated from the evolution of alkaline mantle melts, through exsolution of peraluminous silicate melts from volatile-rich differentiates. It is interesting to note that in the field it is possible to recognize peraluminous silicates melts (e.g., phlogopite-bearing hornblendites) associated with felsic dykes, at least in the northern sector of the IVZ (Finero area). Further investigations are ongoing to constrain if all the historical corundum-rich felsic dykes of IVZ are connected to this process, and to unravel the location and composition of the most primitive melts of such a tectono-magmatic event.

5.4. Survival of Corundum-Bearing Felsic Dykes: The Role of the Refractory Lower Crustal Rocks

Several data and observations related to the felsic dykes here studied are not consistent with a corundum-saturation of the melt through the development of the plumasite-type metasomatic scheme: There is no evidence of an original granitic composition for the migrating melt. The presence of Norian crustal granite has never been documented into the IVZ [53,58,108,109]. Moreover, their occurrence is unexpected, because of the thermal condition of the lower crust had to be well far from those leading to regional anatexis [47,89,110–115]. Generally, the felsic dykes occur within mafic intrusives and granulites and only rarely (the Finero area) they intrude ultramafic rocks.

The strongly positive εHf values documented in zircons from both felsic dykes point to a clear mantle derivation of their parent melts, indicating that chemical exchange with the crustal rocks was

limited. This consideration is also supported by the mantle affinity of the isotopic oxygen composition obtained for corundum from a felsic dyke from Val Sessera (southern IVZ, [15]). A limited interaction with the host crustal rocks is not surprising. Mineral assemblages of IVZ granulites are equilibrated at temperatures >900 °C (~1.0–1.2 GPa; [73,115]), with consequent removal of 30%–40% of granitic component. The gabbroic rocks of the Val Sesia Mafic Complex have equilibrium temperature from 730 °C in the upper part of the intrusive body to 810 °C at the bottom, close to the Insubric line [72]. Nevertheless, the temperature estimated for large dehydration melting of amphibole in mafic rocks is definitely larger (ca. 950 °C; [116]). A completely different scenario is expected in the case that the felsic melts entered in contact with very fertile amphibolite-facies rocks, which during, Norian overlied the granulite-facies rocks. At mid-crustal depth, metapelites and metagreywakes can start melting at temperatures lower than those typical of mantle melts, from 650 to 730 °C under fluid-saturated and fluid-absent conditions, respectively [117,118]. Similar temperatures of beginning of partial melting are shown by carbonates (>600 °C; [119]) and by metabasites under fluid-saturated conditions (680 °C), whereas the temperature of fluid-absent partial melting of metabasites is definitely higher i.e., 850 °C ([116–118,120] and references therein). Besides, the rate of melt production during the partial melting of metapelites, even under fluid-absent conditions, is extremely large at ~820–875 °C, because of the breakdown reaction involving mostly biotite ([116] and references therein, [121]). Thus, it is expected that the composition of relatively small volumes of HT mantle melts rapidly changes, due to intense chemical exchange with amphibolite-facies rocks and/or assimilation of anatectic melts. A spectacular example of the results of this interaction is the formation of garnetite dykes in Val Fiorina (northern IVZ; [122]).

Many reaction schemes and differentiation trends can be envisaged depending on temperature and composition of the intruding melt, the volatile abundance, the depth level and the composition of the basement rocks met by the melt during its ascent. In the specific case of the mantle melts producing the investigated corundum-saturated felsic rocks, as consequence of the volumetric predominance in the basement of metapelites, metagreywackes and metabasites, the interaction with amphibolite-facies rocks would increase the silica content of the melt, progressively promoting the precipitation of plagioclase instead of corundum. This scenario is confirmed by the results of MELTS thermodynamic simulation of Sutherland et al. [76].

It is thus evident that the chance to have the preservation of corundum-saturated intrusive bodies produced by mantle melts differentiation is strongly limited to sequences typically formed by lower crustal rocks, such as refractory granulites and intrusive mafic bodies (Figure 12). This provides an explanation to the rarity of corundum-rich intrusive rocks with respect to the widespread corundum occurrence in alkaline volcanic terrains.

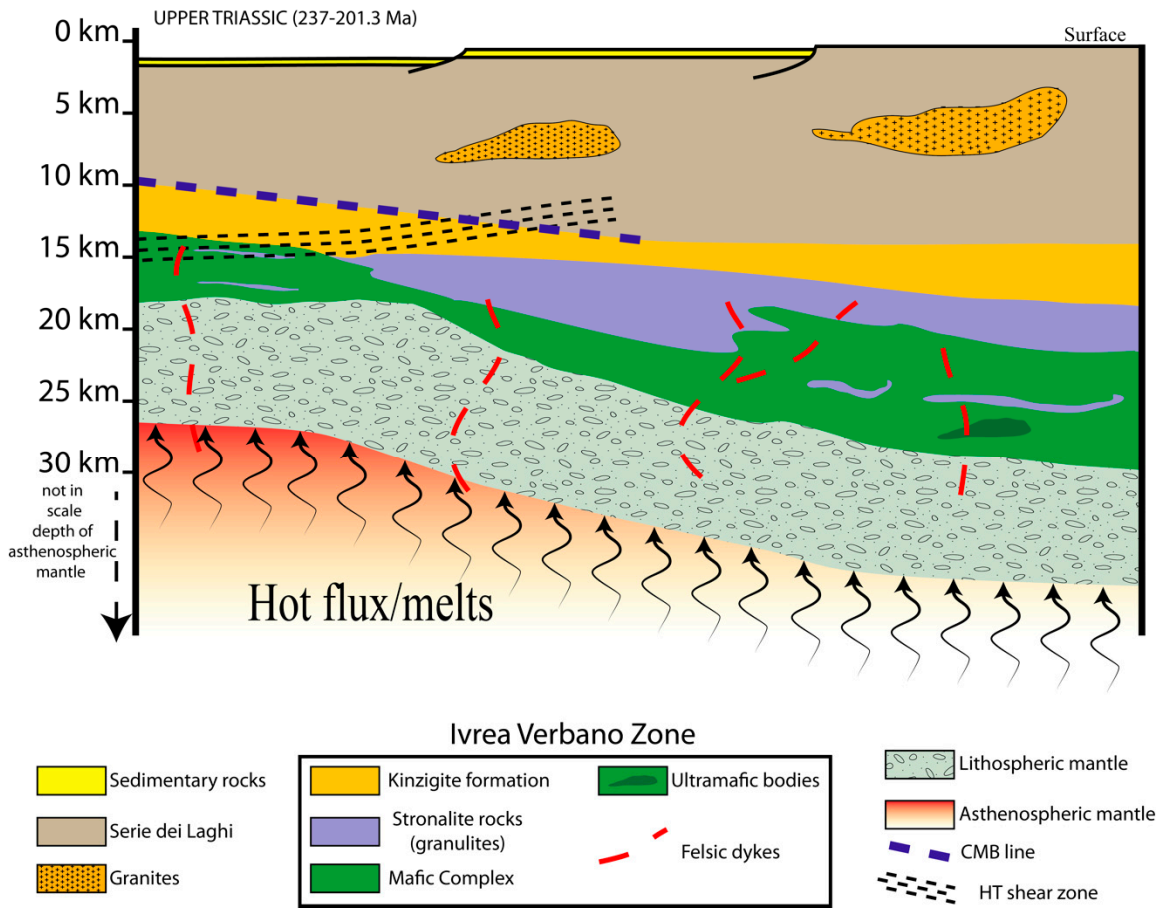

Figure 12. Schematic sketch of the IVZ lithospheric section at Upper Triassic showing the intrusion of felsic dykes in the middle/lower crustal levels. Black arrows indicate the hot flux/melt upraising from asthenosphere in an extensional tectonic regime.

5.5. Geodynamic Implications

In this section, the intrusion of felsic dykes is discussed in the framework of the temperature and time (T-t) evolution of the lower continental crust from Carboniferous to Jurassic (see Figure 13). According to Ewing et al. [115] the T-t history of the lower crust was characterized by a regional HT metamorphism during Carboniferous followed by a peak temperature event at Permian, coeval with large mafic magmatism at the base of the crust (Figure 13). Several heating events occurred in the lower crustal rocks from Permian to Lower Triassic. Discrete heating phenomena were reported by several authors up to Jurassic and were related to hyper-extension during exhumation, e.g., [54,70,115,123,124]. Besides the main mafic magmatism observed in the Sesia Valley occurred at Permian (295–282 Ma; [49,125,126]), the lower crust experienced the intrusion of several discrete bodies at different levels and time (Figure 13). Sills and small mafic bodies occurred in Carboniferous time (i.e., 314 ± 5 Ma and 306 ± 5 Ma for the Monte Capio and Albo sills, respectively; [53]), whereas alkaline ultramafic pipes started to be intruded at least 5 Myr after the formation of the Mafic Complex (i.e., 277 Ma) and possibly continued up to 249 Ma [56]. Important igneous events mark the geodynamic evolution of the area now referred to the Southern Alps during Triassic times. In particular, a diffuse igneous activity with orogenic, shoshonitic to K-rich calc-alkaline, affinity developed during the Middle Triassic (~243–235 Ma) in the Eastern (Dolomites area) and Central (Brescian PreAlps) sectors ([127–132]). These events occurred under mainly trans-tensional regime, which determined the partial melting of mantle regions metasomatized by crustal components during the Variscan orogenic cycle [129–131]. In the westernmost sector of the Southern Alps, the record of

this tectono-magmatic activity is poorly documented, being essentially limited to Ladinian-Carnian ages provided by magmatic (e.g., 239–232 Ma; [60,63,133]) and metamorphic zircons, e.g., [134,135] from the deepest crustal rocks of IVZ, namely those of the Finero Complex, and by zircons from tuffitic layers occurring in the carbonate platform (241 Ma; [132,136]). Alkali-rich magmatism with orogenic character similar to that of Middle Triassic lavas and intrusives of Dolomites has been documented in the Finero Complex by Giovanardi et al. [137].

The Norian zircon ages found in the felsic dykes of this study are significantly younger than those attributed to the magmatic cycles with orogenic affinity. In particular, they match intrusion zircon ages (on average, 225–226 Ma) provided for nepheline-and-sodalite-bearing felsic dykes intruding both the mantle Phlogopite Peridotite [20,21] and the deepest, intrusive crustal units [138,139]. Younger Norian-Pleisbachian ages are given by nepheline-bearing diorites (213–190 Ma; [22]) and other felsic dykes (213 Ma; [64]) intruding the lowermost crustal, intrusive units of Finero Complex. Nepheline-and-sodalite-bearing diorites have anorogenic, alkaline affinity, recording mixture of depleted mantle and high μ (HIMU) isotopic components typical of Ocean Island Basalts (OIB; [20–22]) and convecting "asthenospheric" mantle. These observations induced to consider such a magmatism as a result of a mantle plume activity, involving the upraise and melting of fertile asthenosphere [20–22]. The isotopic Hf composition found in the zircons from the felsic dykes studied here support a derivation of the parental melts from a deep, asthenospheric reservoir with depleted mantle to mildly enriched geochemical signature. A transition of the geochemical affinity from orogenic to anorogenic ("transitional") was also recognized in the 217 Ma melts erupted in the Brescian PreAlps [140]. Recent geochemical and geochronological constraints on lamprophyiric dykes from Dolomites point to 219–220 Ma (Ar-Ar ages) alkaline activity with the involvement OIB-like components [141]. As a whole these observations indicate a regional upwelling of deep-seated asthenosphere over more than 500 km pointing to a possible mantle plume activity. From a structural point of view, the 225–215 Ma time interval records a change of the tectonic regime towards a more real/more authentic/purer extensional environment. It corresponds to the beginning of rifting stages, precursor episodes of the opening of Alpine Tethys. They were associated with the development of sedimentary unconformities in half-graben structures, which accommodated E-W-directed lateral extension [113,142–144], and associated with exhumation of lithospheric mantle of the Adria plate [145]. In the IVZ, this tectonic stage was accommodated by several shear zones at different crustal levels [113,134,146,147]. According to recent geochronological investigations episodic magmatism producing mafic/ultramafic rocks, alkaline dykes/pegmatites and carbonatites (with evidence of crustal assimilation) continued up to Jurassic, likely related discrete episodes of thinning and exhumation (Figure 13; [14,22,57,59,60,62,148]). However, further investigations are needed in order to place more detailed constraints on the mantle-crust interplay ruling the rifting of the continental before the opening of the Alpine Tethys.

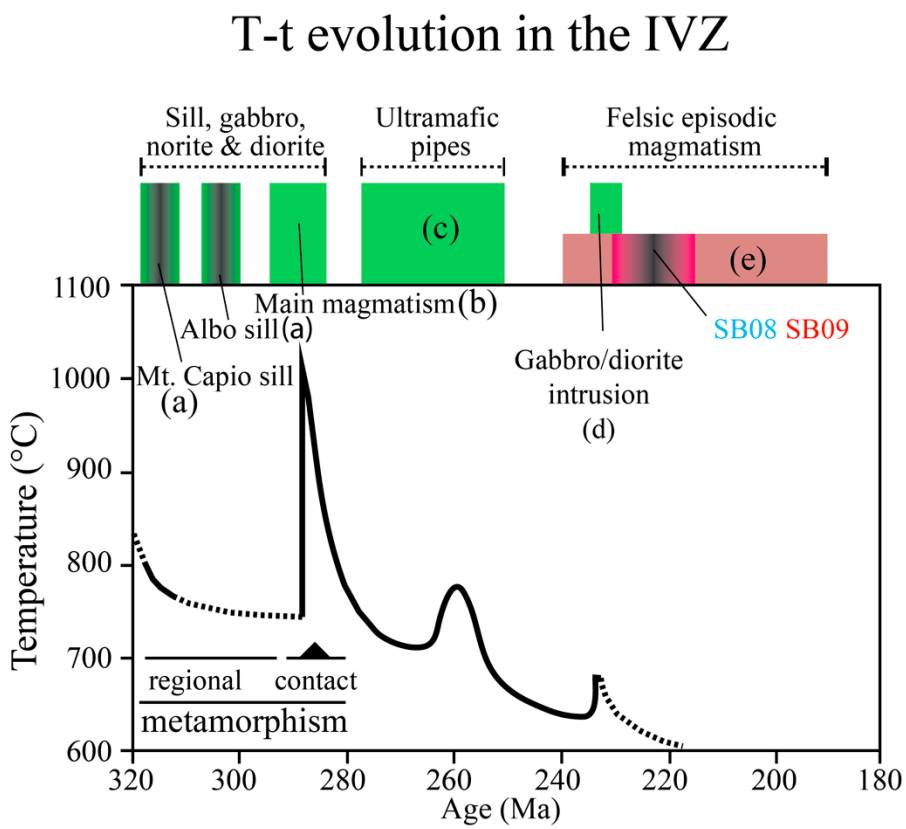

Figure 13. Temperature and time (T-t) plot for the central and southern part of IVZ, modified after Ewing et al. [51,115] and Klötzi et al. [53]. The black line indicates T-t evolution of high-grade metamorphic rocks. Magmatic events occurred in the IVZ from Permian to Jurassic are also shown at the top of the T-t plot. Green and pink boxes refer to zircon $^{206}Pb/^{238}U$ age data from mafic/ultramafic and felsic compositions, respectively. References: (**a**) [53]; (**b**) [49]; (**c**) [51,56,58] (**d**) [60]; (**e**) [14,20,22,62]. The intrusion age for the studied felsic dykes are also shown.

6. Conclusions

Felsic dykes containing large (up to 2 cm) and abundant (up to 50 vol.%) corundum crystals occur within lower crustal rocks of the Ivrea–Verbano Zone. The dykes show either pegmatite-like textures, resulted from magmatic, undisturbed crystallization or porphyroclastic textures due to release of large amounts of volatile-rich components, hydrodynamic fracturing and grain size reduction during late magmatic stages. The Hf isotopic composition of zircon suggests a deep mantle source for the parent melts, which intruded the bottom of the continental Adria crust during the Upper Triassic (223–224 Ma). Major element composition, zircon chemistry and the occurrence of accessory minerals such as Nb-Ta-oxides and uraninites point to a segregation of these felsic dykes from extremely differentiated melts. It is proposed that corundum oversaturation was the consequence of the exsolution of peraluminous silicate melts promoted by volatiles overpressure. Field observations, in combination with petrological, microstructural and geochemical evidence for both felsic dykes and host rocks, suggest that corundum oversaturation in uprising mantle melts can be preserved only in bodies/conduits intruding ultramafic and/or refractory, granulitic crustal rocks, i.e., in lower crust sequences. Triassic magmatic activity is largely documented throughout the Southern Alps, being related to a different tectono-magmatic cycle. In this frame, the magmatism producing corundum-rich felsic dykes marks the beginning of a major reorganization of the tectonic structures of the Southern Alps, during which the trans-tensional deformation regime developed during Middle Triassic (~243–235 MA) in association to orogenic magmatism (with shoshonitic to K-rich calk-alkaline geochemical affinity) evolved towards a more frank extensional environment in the Upper Triassic (~225 Ma), coupled with

anorogenic magmatism fed by large volumes of asthenospheric components. It is argued that such a change in the tectono-magmatic features can represent the actual onset of the Alpine cycle.

Supplementary Materials: The following are available online at http://www.mdpi.com/2076-3263/10/8/281/s1, Table S1. List of analyses made on SB09 and SB08 samples. Table S2. Mineral compositions based on EMPA analyses for both felsic dykes. Table S3. LA-ICP-MS U/Pb data of zircon grains for SB09. Table S4. LA-ICP-MS U/Pb data of zircon grains for SB08. Table S5. LA-ICP-MS trace elements of zircon grains for SB09. Table S6. LA-ICP-MS trace elements of zircon grains for SB08. Table S7. LA–ICP-(MC)-MS Lu/Hf composition of zircon grains for SB09 and SB08. Figure S1. Ternary composition diagram for micas showing the composition of biotite. Red squares show the composition of biotite for SB09 felsic dyke and green squares show the composition of biotite for host gabbro of the SB08 dyke. The pink and orange squares are the composition of biotite and siderophyllite reported in the Handbook of Mineralogy [149]. Figure S2. (a,b) CL and backscattered electron (BSE) images for a zircon grain (SB09) showing internal features (zoning and inclusions) (c,d) RGB images obtained from X-ray maps showing the rich Y, U, Si, P phases/domains included in the zircon grain. (e,f) CL and BSE images for a zircon grain (SB08) showing internal features (zoning and inclusions) (g,h) RGB images obtained from X-ray maps showing the rich Y, U, Si, P phases/domains included in the zircon grain. Figure S3. Chondrite-normalized REE patterns (averages) of zircons from felsic dyke (SB09 and SB08) and from different magmatic rock types reported in Belusova et al. [68]. Normalization values are from McDonough and Sun [69].

Author Contributions: Conceptualized the study, A.L, A.Z.; performed the formal analysis, and data curation, M.B., A.L., S.T. and T.G.; prepared the original initial draft and writing, M.B., A.L. and A.Z.; supervised and provided critical reviews and editing, M.M., E.D., T.G. and S.T. All authors have read and agreed to the published version of the manuscript.

Funding: This research was funded by the following projects: PRIN2015 "Geochemical and isotopic budget of highly metasomatized sub-continental mantle in the Africa and Europe geodynamics systems: modern and fossil analogues"; PRIN2017 "Micro to Macro—how to unravel the nature of the large magmatic events (20178LPCPW- Langone Antonio)". Bonazzi has been supported by the European Research Council (ERC) under the European Union's Horizon 2020 research and innovation programme (grant agreement No 714936 for the project TRUE DEPTHS to M. Alvaro) and by the Italian Ministry of Education, University and Research (MIUR) (PRIN-2017ZE49E7).

Acknowledgments: We thanks Vincenza Guarino and Leone Melluso for the discussions on the feldspars and biotites chemical analyses. Davide Berno is thanked for support with field logistics. We thank and Frederick Lin Sutherlan, Romain Augier and two anonymous reviewers for comments that helped us improve the manuscript.

Conflicts of Interest: The authors declare no conflict of interest.

References

1. Tumiati, S.; Zanchetta, S.; Pellegrino, L.; Ferrario, C.; Casartelli, S.; Malaspina, N. Granulite-facies Overprint in Garnet Peridotites and Kyanite Eclogites of Monte Duria (Central Alps, Italy): Clues from Srilankite-and Sapphirine-Bearing Symplectites. *J. Pet.* **2018**, *59*, 115–151. [CrossRef]
2. Simonet, C.; Fritsch, E.; Lasnier, B. A classification of gem corundum deposits aimed towards gem exploration. *Ore Geol. Rev.* **2008**, *34*, 127–133. [CrossRef]
3. Giuliani, G.; Groat, L.A.; Fallick, A.E.; Pignatelli, I.; Pardieu, V. Ruby Deposits: A Review and Geological Classification. *Minerals* **2020**, *10*, 597. [CrossRef]
4. Liu, T.-C.; Presnall, D.C. Liquidus phase relationships on the join anorthiteforsterite-quartz at 20 kbar with applications to basalt petrogenesis and igneous sapphirine. *Contrib. Miner. Pet.* **1990**, *104*, 735–742. [CrossRef]
5. Sen, G.; Presnall, D.C. Liquidus phase relationships on the join anorthite-forsterite-quartz at 10 kbar with applications to basalt petrogenesis. *Contrib. Miner. Pet.* **1984**, *85*, 404–408. [CrossRef]
6. Lawson, A.C. *Plumasite, an Oligoclase-Corundum Rock near Spanish Peak*; University of California Press: California, CA, USA, 1903.
7. Du Toit, A. Plumasite (corundum-aplite) and titaniferous magnetite rocks from Natal. *S. Afr. J. Geol.* **1918**, *21*, 53–73.
8. Gordon, S.G. Desilicated granitic pegmatites. *P. Acad. Nat. Sci. Phila.* **1921**, *73*, 169–192.
9. Troshin, Y.P. The fluid regime in the formation of rare-metal plumasite granites in Eastern Transbaikalia. *Sov. Geol. Geophys.* **1983**, *24*, 59–67.
10. Peucat, J.; Ruffault, P.; Fritsch, E.; Coz, M.B.-L.; Simonet, C.; Lasnier, B. Ga/Mg ratio as a new geochemical tool to differentiate magmatic from metamorphic blue sapphires. *Lithos* **2007**, *98*, 261–274. [CrossRef]

11. Voudouris, P.; Mavrogonatos, C.; Graham, I.T.; Giuliani, G.; Melfos, V.; Karampelas, S.; Karantoni, V.; Wang, K.; Tarantola, A.; Zaw, K.; et al. Gem Corundum Deposits of Greece: Geology, Mineralogy and Genesis. *Minerals* **2019**, *9*, 49. [CrossRef]
12. Larsen, E.S. A hydrothermal origin of corundum and albitite bodies. *Econ. Geol.* **1928**, *23*, 398–433. [CrossRef]
13. Bertolani, M. La posizione petrogenetica di alcuni filoni corindoniferi della Val Sabbiola (Valsesia). *Rend. Soc. Geol. It.* **1957**, *13*, 120–130.
14. Langone, A.; Padrón-Navarta, J.A.; Ji, W.-Q.; Zanetti, A.; Mazzucchelli, M.; Tiepolo, M.; Giovanardi, T.; Bonazzi, M.; Antonio, L.; Alberto, P.-N.J.; et al. Ductile–brittle deformation effects on crystal-chemistry and U–Pb ages of magmatic and metasomatic zircons from a dyke of the Finero Mafic Complex (Ivrea–Verbano Zone, Italian Alps). *Lithos* **2017**, *284*, 493–511. [CrossRef]
15. Giuliani, G.; Fallick, A.E.; Ohnenstetter, D.; Pegere, G. Oxygen isotopes composition of sapphires from the French Massif Central: Implications for the origin of gem corundum in basaltic fields. *Miner. Deposita* **2008**, *44*, 221–231. [CrossRef]
16. Lelièvre. Mémoire sur un gisement de corindon. *J. Phys. Chim. Hist. Nat.* **1812**, *74-75*, 463–466.
17. Cossa, A. Sul feldspato corindonifero del biellese. *Atti R. Accad. Lincei* **1879**, *3*, 229.
18. Millosevich, F. Le rocce a corindone dell Val Sessera (Prealpi Biellesi). *Atti R. Accad. Lincei* **1927**, *5*, 6–22.
19. Rossi, A. Le rocce corindonifere del "Croso della Gavala" (Valsesia-Vercelli). *Schweiz. Miner. Petrog.* **1968**, *48*, 67–74.
20. Stähle, V.; Frenzel, G.; Kober, B.; Michard, A.; Puchelt, H.; Schneider, W. Zircon syenite pegmatites in the Finero peridotite (Ivrea zone): Evidence for a syenite from a mantle source. *Earth Planet. Sci. Lett.* **1990**, *101*, 196–205. [CrossRef]
21. Stähle, V.; Frenzel, G.; Hess, J.C.; Saupe, F.; Schmidt, S.T.; Schneider, W. Permian metabasalt and Triassic alkaline dykes in the northern Ivrea: Clues to the post-Variscan geodynamic evolution of the Southern Alps. *Schweiz. Miner. Petrog.* **2001**, *81*, 1–21.
22. Schaltegger, U.; Ulianov, A.; Muntener, O.; Ovtcharova, M.; Peytcheva, I.; Vonlanthen, P.; Vennemann, T.; Antognini, M.; Girlanda, F. Megacrystic zircon with planar fractures in miaskite-type nepheline pegmatites formed at high pressures in the lower crust (Ivrea Zone, southern Alps, Switzerland). *Am. Miner.* **2014**, *100*, 83–94. [CrossRef]
23. Zingg, A. The Ivrea and Strona-Ceneri zones (southern Alps, Ticino and N- Italy) - a review. *Schweiz. Miner. Petrog.* **1983**, *63*, 361–392.
24. Sinigoi, S.; Quick, J.E.; Demarchi, G.; Peressini, G. The Sesia Magmatic System. *J. Virtual Explor.* **2010**, *36*, 1–33. [CrossRef]
25. Whitney, D.L.; Evans, B.W. Abbreviations for names of rock-forming minerals. *Am. Miner.* **2009**, *95*, 185–187. [CrossRef]
26. Harley, S.L.; Kelly, N. The impact of zircon–garnet REE distribution data on the interpretation of zircon U–Pb ages in complex high-grade terrains: An example from the Rauer Islands, East Antarctica. *Chem. Geol.* **2007**, *241*, 62–87. [CrossRef]
27. Harley, S.L.; Kelly, N. Zircon Tiny but Timely. *Elements* **2007**, *3*, 13–18. [CrossRef]
28. Tiepolo, M. In situ Pb geochronology of zircon with laser ablation–inductively coupled plasma–sector field mass spectrometry. *Chem. Geol.* **2003**, *199*, 159–177. [CrossRef]
29. Jackson, J.M.; Sinogeikin, S.V.; Carpenter, M.A.; Bass, J.D. Novel phase transition in orthoenstatite. *Am. Miner.* **2004**, *89*, 239–244. [CrossRef]
30. Wiedenbeck, M.; Allé, P.; Corfu, F.; Griffin, W.L.; Meier, M.; Oberli, F.; Von Quadt, A.; Roddick, J.; Spiegel, W. Three natural zircon standards for u-th-pb, lu-hf, trace element and ree analyses. *Geostandard. Newslett.* **1995**, *19*, 1–23. [CrossRef]
31. Sláma, J.; Košler, J.; Condon, D.J.; Crowley, J.L.; Gerdes, A.; Hanchar, J.M.; Horstwood, M.S.A.; Morris, G.A.; Nasdala, L.; Norberg, N.; et al. Plešovice zircon — A new natural reference material for U–Pb and Hf isotopic microanalysis. *Chem. Geol.* **2008**, *249*, 1–35. [CrossRef]
32. Van Achterbergh, E.; Ryan, C.; Griffin, W. *GLITTER On-Line Interactive Data Reduction for the LA-ICPMS Microprobe*; Macquarie Research Ltd.: Sydney, Australia, 2001.
33. Horstwood, M.S.A.; Parrish, R.R.; Nowell, G.; Foster, G.L.; Noble, S. Common-Pb corrected in situ U–Pb accessory mineral geochronology by LA-MC-ICP-MS. *J. Anal. At. Spectrom.* **2003**, *18*, 837. [CrossRef]

34. Ludwig, K.R. *Isoplot 3.00: A Geochronological Toolkit for Microsoft Excel*; Berkeley Geochronology Center Special Publication: Berkeley, CA, USA, 2003; Volume 4, p. 70.
35. Giovanardi, T.; Mazzucchelli, M.; Lugli, F.; Girardi, V.A.; Correia, C.; Tassinari, C.C.; Cipriani, A. Isotopic constraints on contamination processes in the Tonian Goiás Stratiform Complex. *Lithos* **2018**, *310*, 136–152. [CrossRef]
36. Giovanardi, T.; Lugli, F. The Hf-INATOR: A free data reduction spreadsheet for Lu/Hf isotope analysis. *Earth Sci. Inform.* **2017**, *10*, 517–523. [CrossRef]
37. Matteini, M.; Dantas, E.L.; Pimentel, M.M.; Buhn, B. Combined U-Pb and Lu-Hf isotope analyses by laser ablation MC-ICP-MS: Methodology and applications. *An. Acad. Bras. Ciênc.* **2010**, *82*, 479–491. [CrossRef]
38. Blichert-Toft, J.; Albarede, F. The Lu-Hf isotope geochemistry of chondrites and the evolution of the mantle-crust system. *Earth Planet. Sci. Lett.* **1997**, *148*, 243–258. [CrossRef]
39. Connolly, J.A. Computation of phase equilibria by linear programming: A tool for geodynamic modeling and its application to subduction zone decarbonation. *Earth Planet. Sci. Lett.* **2005**, *236*, 524–541. [CrossRef]
40. Holland, T.J.B.; Powell, R. An internally consistent thermodynamic data set for phases of petrological interest. *J. Metamorph. Geol.* **2004**, *16*, 309–343. [CrossRef]
41. Schmid, S.M.; Raumer, J.F. Ivrea Zone and Adjacent Southern Alpine Basement. In *Pre-Mesozoic Geology in the Alps*; Springer Science and Business Media LLC: Berlin/Heidelberg, Germany, 1993; pp. 567–583. [CrossRef]
42. Boriani, A.; Burlini, L.; Sacchi, R. The Cossato-Mergozzo-Brissago Line and the Pogallo Line (Southern Alps, Northern Italy) and their relationships with the late-Hercynian magmatic and metamorphic events. *Tectonophysics* **1990**, *182*, 91–102. [CrossRef]
43. Boriani, A.C.; Villa, I.M. Geochronology of regional metamorphism in the Ivrea-Verbano Zone and Serie dei Laghi, Italian Alps. *Schweiz. Miner. Petrog.* **1997**, *77*, 381–401. [CrossRef]
44. Mulch, A.; Rosenau, M.; Dörr, W.; Handy, M.R. The age and structure of dikes along the tectonic contact of the Ivrea-Verbano and Strona-Ceneri Zones (Southern Alps, Northern Italy, Switzerland). *Schweiz. Miner. Petrog.* **2002**, *82*, 55–76.
45. Hodges, K.V.; Fountain, D.M. Pogallo Line, South Alps, northern Italy: An intermediate crystal level, low-angle normal fault? *Geology* **1984**, *12*, 151. [CrossRef]
46. Zingg, A.; Handy, M.; Hunziker, J.; Schmid, S. Tectonometamorphic history of the Ivrea Zone and its relationship to the crustal evolution of the Southern Alps. *Tectonophysics* **1990**, *182*, 169–192. [CrossRef]
47. Schmid, R.; Wood, B.J. Phase relationships in granulitic metapelites from the Ivrea-Verbano zone (Northern Italy). *Contrib. Miner. Pet.* **1976**, *54*, 255–279. [CrossRef]
48. Henk, A.; Franz, L.; Teufel, S.; Oncken, O. Magmatic Underplating, Extension, and Crustal Reequilibration: Insights From A Cross-Section Through the Ivrea Zone and Strona-Ceneri Zone, Northern Italy. *J. Geol.* **1997**, *105*, 367–378. [CrossRef]
49. Peressini, G.; Quick, J.E.; Sinigoi, S.; Hofmann, A.W.; Fanning, C.M. Duration of a Large Mafic Intrusion and Heat Transfer in the Lower Crust: A SHRIMP U-Pb Zircon Study in the Ivrea-Verbano Zone (Western Alps, Italy). *J. Pet.* **2007**, *48*, 1185–1218. [CrossRef]
50. Rivalenti, G.; Garuti, G.; Rossi, A. The origin of the Ivrea-Verbano basic formation (western italian Alps) - whole rock geochemistry. *Boll. Soc. Geol. Ital.* **1975**, *94*, 1149–1186.
51. Ewing, T.; Hermann, J.; Rubatto, D.; Hermann, J. The robustness of the Zr-in-rutile and Ti-in-zircon thermometers during high-temperature metamorphism (Ivrea-Verbano Zone, northern Italy). *Contrib. Miner. Pet.* **2012**, *165*, 757–779. [CrossRef]
52. Kunz, B.E.; Manzotti, P.; Von Niederhäusern, B.; Engi, M.; Darling, J.R.; Giuntoli, F.; Lanari, P. Permian high-temperature metamorphism in the Western Alps (NW Italy). *Acta Diabetol.* **2017**, *107*, 203–229. [CrossRef]
53. Klötzli, U.S.; Sinigoi, S.; Quick, J.E.; Demarchi, G.; Tassinari, C.C.; Sato, K.; Günes, Z. Duration of igneous activity in the Sesia Magmatic System and implications for high-temperature metamorphism in the Ivrea–Verbano deep crust. *Lithos* **2014**, *206*, 19–33. [CrossRef]
54. Karakas, O.; Wotzlaw, J.-F.; Guillong, M.; Ulmer, P.; Brack, P.; Economos, R.; Bergantz, G.W.; Sinigoi, S.; Bachmann, O. The pace of crustal-scale magma accretion and differentiation beneath silicic caldera volcanoes. *Geology* **2019**, *47*, 719–723. [CrossRef]
55. Garuti, G.; Bea, F.; Zaccarini, F.; Montero, P. Age, Geochemistry and Petrogenesis of the Ultramafic Pipes in the Ivrea Zone, NW Italy. *J. Pet.* **2001**, *42*, 433–457. [CrossRef]

56. Locmelis, M.; Fiorentini, M.L.; Rushmer, T.; Arevalo, R.; Adam, J.; Denyszyn, S.W. Sulfur and metal fertilization of the lower continental crust. *Lithos* **2016**, *244*, 74–93. [CrossRef]
57. Denyszyn, S.W.; Fiorentini, M.; Maas, R.; Dering, G. A bigger tent for CAMP. *Geology* **2018**, *46*, 823–826. [CrossRef]
58. Fiorentini, M.; Laflamme, C.; Denyszyn, S.W.; Mole, D.; Maas, R.; Locmelis, M.; Caruso, S.; Bui, T.-H. Post-collisional alkaline magmatism as gateway for metal and sulfur enrichment of the continental lower crust. *Geoch. Cosmochim. Ac.* **2018**, *223*, 175–197. [CrossRef]
59. Galli, A.; Grassi, D.; Sartori, G.; Gianola, O.; Burg, J.-P.; Schmidt, M. Jurassic carbonatite and alkaline magmatism in the Ivrea zone (European Alps) related to the breakup of Pangea. *Geology* **2019**, *47*, 199–202. [CrossRef]
60. Zanetti, A.; Mazzucchelli, M.; Sinigoi, S.; Giovanardi, T.; Peressini, G.; Fanning, C.M. SHRIMP U-Pb Zircon Triassic Intrusion Age of the Finero Mafic Complex (Ivrea-Verbano Zone, Western Alps) and its Geodynamic Implications. *J. Pet.* **2013**, *54*, 2235–2265. [CrossRef]
61. Von Quadt, A.; Ferrario, A.; Diella, V.; Hansmann, W.; Vavra, G.; Koeppel, V. U–Pb ages of zircons from chromitites of the phlogopite peridotite of Finero Ivrea zone, northern Italy. *Schweiz. Miner. Petrog.* **1993**, *73*, 137–138.
62. Grieco, G.; Ferrario, A.; Von Quadt, A.; Koeppel, V.; Mathez, E.A. The Zircon-Bearing Chromitites of the Phlogopite Peridotite of Finero (Ivrea Zone, Southern Alps): Evidence and Geochronology of a Metasomatized Mantle Slab. *J. Pet.* **2001**, *42*, 89–101. [CrossRef]
63. Hingerl, F.; Klötzli, U.; Steuber, C.; Kleinschrodt, R. New results from the mafic complex in the Finero area. In Proceedings of the 33th International Geological Congress, Oslo, Norway, 6–14 August 2008; pp. 6–14.
64. Oppizzi, P.; Schaltegger, U. Zircon-bearing plagioclasites from the Finero complex (Ivrea zone): Dating a Late Triassic mantle hic-cup. *Schweiz. Miner. Petrog.* **1999**, *79*, 330–331.
65. Hoek, J.D. A classification of dyke-fracture geometry with examples from Precambrian dyke swarms in the Vestfold Hills, Antarctica. *Geol. Rundsch.* **1991**, *80*, 233–248. [CrossRef]
66. Vermeesch, P. IsoplotR: A free and open toolbox for geochronology. *Geosci. Front.* **2018**, *9*, 1479–1493. [CrossRef]
67. Guo, J.; O'Reilly, S.Y.; Griffin, W.L. Zircon inclusions in corundum megacrysts: I. Trace element geochemistry and clues to the origin of corundum megacrysts in alkali basalts. *Geochim. Cosmochim. Acta* **1996**, *60*, 2347–2363. [CrossRef]
68. Belousova, E.; Griffin, W.L.; O'Reilly, S.Y.; Fisher, N. Igneous zircon: Trace element composition as an indicator of source rock type. *Contrib. Miner. Pet.* **2002**, *143*, 602–622. [CrossRef]
69. McDonough, W.F. The Composition of the Earth. *Int. Geophys.* **2001**, *76*, 3–23. [CrossRef]
70. Zanetti, A.; Giovanardi, T.; Langone, A.; Tiepolo, M.; Wu, F.-Y.; Dallai, L.; Mazzucchelli, M. Origin and age of zircon-bearing chromitite layers from the Finero phlogopite peridotite (Ivrea–Verbano Zone, Western Alps) and geodynamic consequences. *Lithos* **2016**, *262*, 58–74. [CrossRef]
71. Malitch, K.; Belousova, E.; Griffin, W.L.; Badanina, I.; Knauf, V.; O'Reilly, S.Y.; Pearson, N. Laurite and zircon from the Finero chromitites (Italy): New insights into evolution of the subcontinental mantle. *Ore Geol. Rev.* **2017**, *90*, 210–225. [CrossRef]
72. Demarchi, G.; Quick, J.E.; Sinigoi, S.; Mayer, A. Pressure Gradient and Original Orientation of A Lower-Crustal Intrusion in the Ivrea-Verbano Zone, Northern Italy. *J. Geol.* **1998**, *106*, 609–622. [CrossRef]
73. Redler, C.; Johnson, T.E.; White, R.; Kunz, B.E. Phase equilibrium constraints on a deep crustal metamorphic field gradient: Metapelitic rocks from the Ivrea Zone (NW Italy). *J. Metamorph. Geol.* **2011**, *30*, 235–254. [CrossRef]
74. Redler, C.; White, R.; Johnson, T.E. Migmatites in the Ivrea Zone (NW Italy): Constraints on partial melting and melt loss in metasedimentary rocks from Val Strona di Omegna. *Lithos* **2013**, *175*, 40–53. [CrossRef]
75. Coenraads, R.R.; Sutherland, F.L.; Kinny, P.D. The origin of sapphires: U–Pb dating of zircon inclusions sheds new light. *Miner. Mag.* **1990**, *54*, 113–122. [CrossRef]
76. Sutherland, F.L.; Hoskin, P.W.O.; Fanning, C.M.; Coenraads, R.R. Models of corundum origin from alkali basaltic terrains: A reappraisal. Contrib. *Miner. Pet.* **1998**, *133*, 356–372. [CrossRef]
77. Baldwin, L.; Tomaschek, F.; Ballhaus, C.; Gerdes, A.; Fonseca, R.O.C.; Geisler, T.; Nagel, T.; Wirth, R. Petrogenesis of alkaline basalt-hosted sapphire megacrysts. Petrological and geochemical investigations of

in situ sapphire occurrences from the Siebengebirge Volcanic Field, Germany. *Contrib. Miner. Pet.* **2017**, *172*, 43. [CrossRef]
78. Mazzucchelli, M. The Classification of Igneous Rocks: Diorite vs. Syenite–A suggestion in order to avoid a contradiction. *Episodes* **2016**, *39*, 524–525. [CrossRef] [PubMed]
79. Sørensen, H.; Bailey, J.C.; Rose-Hansen, J. The emplacement and crystallization of the U–Th–REE-rich agpaitic and hyperagpaitic lujavrites at Kvanefjeld, Ilímaussaq alkaline complex, South Greenland. *B. Geol. Soc. Den.* **2011**, *59*, 69–92.
80. Waters, F.G. A suggested origin of MARID xenoliths in kimberlites by high pressure crystallization of an ultrapotassic rock such as lamproite. *Contrib. Miner. Pet.* **1987**, *95*, 523–533. [CrossRef]
81. Dawson, J.; Smith, J.V. The MARID (mica-amphibole-rutile-ilmenite-diopside) suite of xenoliths in kimberlite. *Geochim. Cosmochim. Acta* **1977**, *41*, 309–323. [CrossRef]
82. Konzett, J.; Armstrong, R.A.; Sweeney, R.J.; Compston, W. The timing of MARID metasomatism in the Kaapvaal mantle: An ion probe study of zircons from MARID xenoliths. *Earth Planet. Sci. Lett.* **1998**, *160*, 133–145. [CrossRef]
83. Price, R.C.; Cooper, A.F.; Woodhead, J.D.; Cartwright, I. Phonolitic Diatremes within the Dunedin Volcano, South Island, New Zealand. *J. Pet.* **2003**, *44*, 2053–2080. [CrossRef]
84. Pidgeon, R.T.; Nemchin, A.A.; Hitchen, G.J. Internal structures of zircons from Archaean granites from the Darling Range batholith: Implications for zircon stability and the interpretation of zircon U-Pb ages. *Contrib. Miner. Pet.* **1998**, *132*, 288–299. [CrossRef]
85. Schaltegger, U.; Fanning, C.M.; Günther, D.; Maurin, J.C.; Schulmann, K.; Gebauer, D. Growth, annealing and recrystallization of zircon and preservation of monazite in high-grade metamorphism: Conventional and in-situ U-Pb isotope, cathodoluminescence and microchemical evidence. *Contrib. Miner. Pet.* **1999**, *134*, 186–201. [CrossRef]
86. Corfu, F.; Hanchar, J.M.; Hoskin, P.W.O.; Kinny, P. Atlas of Zircon Textures. *Rev. Miner. Geochem.* **2003**, *53*, 469–500. [CrossRef]
87. Pidgeon, R.T. Recrystallisation of oscillatory zoned zircon: Some geochronological and petrological implications. *Contrib. Miner. Pet.* **1992**, *110*, 463–472. [CrossRef]
88. Brodie, K.; Rutter, E.H. Deep crustal extensional faulting in the Ivrea Zone of Northern Italy. *Tectonophysics* **1987**, *140*, 193–212. [CrossRef]
89. Handy, M. The structure, age and kinematics of the Pogallo Fault Zone; Southern Alps, northwestern Italy. *Eclogae Geol. Helv.* **1987**, *80*, 593–632.
90. Irving, A.J. Polybaric magma mixing in alkali basalts and kimberlites: Evidence from corundum, zircon and ilmenite megacrysts. In Proceedings of the 4th International Kimberlite Conference, Perth, Australia, 19 September 1986; 1, pp. 262–264. [CrossRef]
91. Coenraads, R.R.; Vichit, P.; Sutherland, F.L. An unusual sapphire–zircon–magnetite xenolith from the Chanthaburi Gem Province, Thailand. *Miner. Mag.* **1995**, *59*, 465–479. [CrossRef]
92. Guo, J.; O'Reilly, S.Y.; Griffin, W.L. Corundum from basaltic terrains: A mineral inclusion approach to the enigma. *Contrib. Miner. Pet.* **1996**, *122*, 368–386. [CrossRef]
93. Aspen, P.; Upton, B.G.; Dickin, A.P. Anorthoclase, sanidine and associated megacrysts in Scottish alkali basalts: High-pressure syenitic debris from upper mantle sources? *Eur. J. Miner.* **1990**, *2*, 503–518. [CrossRef]
94. Barboza, S.A.; Bergantz, G.W. Metamorphism and Anatexis in the Mafic Complex Contact Aureole, Ivrea Zone, Northern Italy. *J. Pet.* **2000**, *41*, 1307–1327. [CrossRef]
95. Sorokina, E.; Karampelas, S.; Nishanbaev, T.P.; Nikandrov, S.N.; Semiannikov, B.S. Sapphire Megacrysts In Syenite Pegmatites From the Ilmen Mountains, South Urals, Russia: New Mineralogical Data. *Can. Miner.* **2017**, *55*, 823–843. [CrossRef]
96. Monchoux, P.; Fontan, F.; De Parseval, P.; Martin, R.F.; Wang, R.C. Igneous albitite dikes in orogenic lherzolites, western Pyrénées, France: A possible source for corundum and alkali feldspar xenocrysts in basaltic terranes. I. Mineralogical associations. *Can. Mineral.* **2006**, *44*, 817–842. [CrossRef]
97. Pin, C.; Monchoux, P.; Paquette, J.L.; Azambre, B.; Wang, R.C.; Martin, R.F. Igneous albitite dikes in orogenic lherzolites, western Pyrénées, France: A possible source for corundum and alkali feldspar xenocrysts in basaltic terranes. II. Geochemical and petrogenetic considerations. *Can. Mineral.* **2006**, *44*, 843–856. [CrossRef]

98. Irving, A.J.; Frey, F.A.; Frey, F. Trace element abundances in megacrysts and their host basalts: Constraints on partition coefficients and megacryst genesis. *Geochim. Cosmochim. Acta* **1984**, *48*, 1201–1221. [CrossRef]
99. Upton, B.G.J.; Hinton, R.W.; Aspen, P.; Finch, A.; Valley, J.W.; Tatsumi, Y.; Arai, R.; Ishizaka, K. Megacrysts and Associated Xenoliths: Evidence for Migration of Geochemically Enriched Melts in the Upper Mantle beneath Scotland. *J. Pet.* **1999**, *40*, 935–956. [CrossRef]
100. Giovanardi, T.; Morishita, T.; Zanetti, A.; Mazzucchelli, M.; Vannucci, R. Igneous sapphirine as a product of melt-peridotite interactions in the Finero Phlogopite-Peridotite Massif, Western Italian Alps. *Eur. J. Miner.* **2013**, *25*, 17–31. [CrossRef]
101. Green, D. Experimental petrology of peridotites, including effects of water and carbon on melting in the Earth's upper mantle. *Phys. Chem. Miner.* **2015**, *42*, 95–122. [CrossRef]
102. Izokh, A.; Smirnov, S.; Egorova, V.; Anh, T.T.; Kovyazin, S.; Phuong, N.T.; Kalinina, V. The conditions of formation of sapphire and zircon in the areas of alkali-basaltoid volcanism in Central Vietnam. *Russ. Geol. Geophys.* **2010**, *51*, 719–733. [CrossRef]
103. Zanetti, A.; Mazzucchelli, M.; Rivalenti, G.; Vannucci, R. The Finero phlogopite-peridotite massif: An example of subduction-related metasomatism. *Contrib. Miner. Pet.* **1999**, *134*, 107–122. [CrossRef]
104. Morishita, T.; Arai, S.; Ishida, Y. Occurrence and chemical composition of amphiboles and related minerals in corundum-bearing mafic rock from the Horoman Peridotite Complex, Japan. *Lithos* **2007**, *95*, 425–440. [CrossRef]
105. Thomas, R.; Webster, J.; Rhede, D.; Seifert, W.; Rickers, K.; Förster, H.-J.; Heinrich, W.; Davidson, P. The transition from peraluminous to peralkaline granitic melts: Evidence from melt inclusions and accessory minerals. *Lithos* **2006**, *91*, 137–149. [CrossRef]
106. Thomas, R.; Davidson, P. Water and melt/melt immiscibility, the essential components in the formation of pegmatites; evidence from melt inclusions. *Z. Geol. Wiss. Berl.* **2008**, *36*, 347–364.
107. Simmons, W.B.; Webber, K.L. Pegmatite genesis: State of the art. *Eur. J. Miner.* **2008**, *20*, 421–438. [CrossRef]
108. Vavra, G.; Gebauer, D.; Schmid, R.; Compston, W. Multiple zircon growth and recrystallization during polyphase Late Carboniferous to Triassic metamorphism in granulites of the Ivrea Zone (Southern Alps): An ion microprobe (SHRIMP) study. *Contrib. Miner. Pet.* **1996**, *122*, 337–358. [CrossRef]
109. Guergouz, C.; Martin, L.; Vanderhaeghe, O.; Thébaud, N.; Fiorentini, M. Zircon and monazite petrochronologic record of prolonged amphibolite to granulite facies metamorphism in the Ivrea-Verbano and Strona-Ceneri Zones, NW Italy. *Lithos* **2018**, *308*, 1–18. [CrossRef]
110. Handy, M.R.; Franz, L.; Heller, F.; Janott, B.; Zurbriggen, R. Multistage accretion and exhumation of the continental crust (Ivrea crustal section, Italy and Switzerland). *Tectonics* **1999**, *18*, 1154–1177. [CrossRef]
111. Schmid, S.; Zingg, A.; Handy, M. The kinematics of movements along the Insubric Line and the emplacement of the Ivrea Zone. *Tectonophysics* **1987**, *135*, 47–66. [CrossRef]
112. Rutter, E.H.; Brodie, K.; James, T.; Blundell, D.J.; Waltham, D.A. Seismic Modeling of Lower and Mid-Crustal Structure as Exemplified by the Massiccio dei Laghi (Ivrea-Verbano Zone and Serie dei Laghi) Crustal Section, Northwestern Italy. In *Heterogeneity in the Crust and Upper Mantle*; Springer Science and Business Media LLC: Boston, MA, USA, 2003; pp. 67–97. [CrossRef]
113. Siegesmund, S.; Layer, P.; Dunkl, I.; Vollbrecht, A.; Steenken, A.; Wemmer, K.; Ahrendt, H. Exhumation and deformation history of the lower crustal section of the Valstrona di Omegna in the Ivrea Zone, southern Alps. *Geol. Soc. Lond. Spéc. Publ.* **2008**, *298*, 45–68. [CrossRef]
114. Beltrando, M.; Stockli, D.F.; Decarlis, A.; Manatschal, G. A crustal-scale view at rift localization along the fossil Adriatic margin of the Alpine Tethys preserved in NW Italy. *Tectonics* **2015**, *34*, 1927–1951. [CrossRef]
115. Ewing, T.; Rubatto, D.; Beltrando, M.; Hermann, J.; Hermann, J. Constraints on the thermal evolution of the Adriatic margin during Jurassic continental break-up: U–Pb dating of rutile from the Ivrea–Verbano Zone, Italy. *Contrib. Miner. Pet.* **2015**, *169*, 44. [CrossRef]
116. Annen, C.; Blundy, J.D.; Sparks, R.S.J. The Genesis of Intermediate and Silicic Magmas in Deep Crustal Hot Zones. *J. Pet.* **2005**, *47*, 505–539. [CrossRef]
117. Wolf, M.B.; Wyllie, P.J. Dehydration-melting of amphibolite at 10 kbar: The effects of temperature and time. *Contrib. Miner. Pet.* **1994**, *115*, 369–383. [CrossRef]
118. Vielzeuf, D. Melting relations in hydrous systems revisited: Application to metapelites, metagreywackes and metabasalts. *Contrib. Mineral. Petr.* **2001**, *141*, 251–267. [CrossRef]

119. Floess, D.; Baumgartner, L.P.; Vonlanthen, P. An observational and thermodynamic investigation of carbonate partial melting. *Earth Planet. Sci. Lett.* **2015**, *409*, 147–156. [CrossRef]
120. Peto, P. An experimental investigation of melting relations involving muscovite and paragonite in the silica-saturated portion of the system K2O-NA2O-AL2O3-SIO2-H2O to 15 kb total pressure: Progress in Experimental Petrology. *Nat. Environ. Res. Counc. Pubbl.* **1976**, *4*, 41–45.
121. Vielzeuf, D.; Holloway, J.R. Experimental determination of the fluid-absent melting relations in the pelitic system. *Contrib. Miner. Pet.* **1988**, *98*, 257–276. [CrossRef]
122. Rivalenti, G.; Vannucci, R.; Rampone, E.; Mazzucchelli, M.; Piccardo, G.B.; Piccirillo, E.M.; Bottazzi, P.; Ottolini, L. Peridotite clinopyroxene chemistry reflects mantle processes rather than continental versus oceanic settings. *Earth Planet. Sci. Lett.* **1996**, *139*, 423–437. [CrossRef]
123. Smye, A.J.; Stockli, D.F. Rutile U–Pb age depth profiling: A continuous record of lithospheric thermal evolution. *Earth Planet. Sci. Lett.* **2014**, *408*, 171–182. [CrossRef]
124. Smye, A.J.; Lavier, L.L.; Zack, T.; Stockli, D.F. Episodic heating of continental lower crust during extension: A thermal modeling investigation of the Ivrea-Verbano Zone. *Earth Planet. Sci. Lett.* **2019**, *521*, 158–168. [CrossRef]
125. Quick, J.; Sinigoi, S.; Peressini, G.; Demarchi, G.; Wooden, J.; Sbisà, A. Magmatic plumbing of a large Permian caldera exposed to a depth of 25 km. *Geology* **2009**, *37*, 603–606. [CrossRef]
126. Sinigoi, S.; Quick, J.E.; Demarchi, G.; Klötzli, U. The role of crustal fertility in the generation of large silicic magmatic systems triggered by intrusion of mantle magma in the deep crust. *Contrib. Miner. Pet.* **2011**, *162*, 691–707. [CrossRef]
127. Bonadiman, C.; Coltorti, M.; Siena, F. Petrogenesis and T-fO2 estimates of Mt. Monzoni complex (Central Dolomites, Southern Alps): A Triassic shoshonitic intrusion in a transcurrent geodynamic setting. *Eur. J. Miner.* **1994**, *6*, 943–966. [CrossRef]
128. Cassinis, G.; Nicosia, U.; Pittau, P.; Ronchi, A. Palaeontological and radiometric data from the Permian continental deposits of the Central-Eastern Southern Alps (Italy), and their stratigraphic implications. *Mém. l'Assoc. Géologues Permien* **2002**, *2*, 53–74.
129. Casetta, F.; Coltorti, M.; Ickert, R.B.; Bonadiman, C.; Giacomoni, P.P.; Ntaflos, T. Intrusion of shoshonitic magmas at shallow crustal depth: T–P path, H2O estimates, and AFC modeling of the Middle Triassic Predazzo Intrusive Complex (Southern Alps, Italy). *Contrib. Miner. Pet.* **2018**, *173*, 57. [CrossRef]
130. Lustrino, M.; Abbas, H.; Agostini, S.; Caggiati, M.; Carminati, E.; Gianolla, P. Origin of Triassic magmatism of the Southern Alps (Italy): Constraints from geochemistry and Sr-Nd-Pb isotopic ratios. *Gondwana Res.* **2019**, *75*, 218–238. [CrossRef]
131. De Min, A.; Velicogna, M.; Ziberna, L.; Chiaradia, M.; Alberti, A.; Marzoli, A. Triassic magmatism in the European Southern Alps as an early phase of Pangea break-up. *Geol. Mag.* **2020**, 1–23. [CrossRef]
132. Storck, J.-C.; Wotzlaw, J.-F.; Karakas, Ö.; Brack, P.; Gerdes, A.; Ulmer, P. Hafnium isotopic record of mantle-crust interaction in an evolving continental magmatic system. *Earth Planet. Sci. Lett.* **2020**, *535*, 116100. [CrossRef]
133. Gebauer, D.; Raumer, J.F. The Pre-Alpine Evolution of the Continental Crust of the Central Alps—An Overview. In *Pre-Mesozoic Geology in the Alps*; Springer Science and Business Media LLC: Berlin, Germany, 1993; pp. 93–117.
134. Langone, A.; Tiepolo, M. U-Th-Pb "multi-phase" approach to the study of crystalline basement: Application to the northernmost sector of the Ivrea-Verbano Zone (Alps). *Period. Mineral.* **2015**, *84*, 633–655. [CrossRef]
135. Langone, A.; Zanetti, A.; Daczko, N.R.; Piazolo, S.; Tiepolo, M.; Mazzucchelli, M. Zircon U-Pb Dating of a Lower Crustal Shear Zone: A Case Study From the Northern Sector of the Ivrea-Verbano Zone (Val Cannobina, Italy). *Tectonics* **2018**, *37*, 322–342. [CrossRef]
136. Mundil, R.; Brack, P.; Meier, M.; Rieber, H.; Oberli, F. High resolution U–Pb dating of Middle Triassic volcaniclastics: Time-scale calibration and verification of tuning parameters for carbonate sedimentation. *Earth Planet. Sci. Lett.* **1996**, *141*, 137–151. [CrossRef]
137. Giovanardi, T.; Zanetti, A.; Dallai, L.; Morishita, T.; Hémond, C.; Mazzucchelli, M. Evidence of subduction-related components in sapphirine-bearing gabbroic dykes (Finero phlogopite–peridotite): Insights into the source of the Triassic–Jurassic magmatism at the Europe–Africa boundary. *Lithos* **2020**, *356–357*, 105366. [CrossRef]

138. Klötzli, U.; Hochleitner, R.; Kosler, J. Lower Triassic mantle-derived magmatism in the Ivrea-Verbano Zone: Evidence from laser ablation U–Pb dating of a pegmatite from the eastern Finero Complex (Switzerland). *Mitt. Osterr. Mineral. G.* **2007**, *153*, 53.
139. Klötzli, U.; Klötzli, E.; Günes, Z.; Košler, J. Accuracy of Laser Ablation U-Pb Zircon Dating: Results from a Test Using Five Different Reference Zircons. *Geostand. Geoanal: Res.* **2009**, *33*, 5–15. [CrossRef]
140. Cassinis, G.; Durand, M.; Ronchi, A. Reply to discussion on the article "Remarks on the Permian-Triassic transition in Central and Eastern Lombardy (Southern Alps, Italy)". *J. Iber. Geol.* **2009**, *35*, 73–78. [CrossRef]
141. Casetta, F.; Ickert, R.B.; Mark, D.F.; Bonadiman, C.; Giacomoni, P.P.; Ntaflos, T.; Coltorti, M. The Alkaline Lamprophyres of the Dolomitic Area (Southern Alps, Italy): Markers of the Late Triassic Change from Orogenic-like to Anorogenic Magmatism. *J. Pet.* **2019**, *60*, 1263–1298. [CrossRef]
142. Winterer, A.B.E.L. Subsidence and Sedimentation on Jurassic Passive Continental Margin, Southern Alps, Italy. *AAPG Bull.* **1981**, *65*, 394–421. [CrossRef]
143. Bertotti, G.; Picotti, V.; Bernoulli, D.; Castellarin, A. From rifting to drifting: Tectonic evolution of the South-Alpine upper crust from the Triassic to the Early Cretaceous. *Sediment. Geol.* **1993**, *86*, 53–76. [CrossRef]
144. Bertotti, G.; Wijbrans, J.; Ter Voorde, M.; Hurford, A.J.; Seward, D. Crustal thermal regime prior to, during, and after rifting: A geochronological and modeling study of the Mesozoic South Alpine rifted margin. *Tectonics* **1999**, *18*, 185–200. [CrossRef]
145. Montanini, A.; Tribuzio, R.; Anczkiewicz, R. Exhumation History of a Garnet Pyroxenite-bearing Mantle Section from a Continent-Ocean Transition (Northern Apennine Ophiolites, Italy). *J. Pet.* **2006**, *47*, 1943–1971. [CrossRef]
146. Brodie, K.H.; Rutter, E.H.; Rex, D. On the age of deep crustal extensional faulting in the Ivrea zone, northern Italy. *Geol. Soc. Lond. Spéc. Publ.* **1989**, *45*, 203–210. [CrossRef]
147. Corvò, S.; Langone, A.; Padrón-Navarta, J.; Tommasi, A.; Zanetti, A. Porphyroclasts: Source and Sink of Major and Trace Elements During Deformation-Induced Metasomatism (Finero, Ivrea-Verbano Zone, Italy). *Geosciences* **2020**, *10*, 196. [CrossRef]
148. Mazzucchelli, M.; Zanetti, A.; Rivalenti, G.; Vannucci, R.; Correia, C.; Tassinari, C.C. Age and geochemistry of mantle peridotites and diorite dykes from the Baldissero body: Insights into the Paleozoic–Mesozoic evolution of the Southern Alps. *Lithos* **2010**, *119*, 485–500. [CrossRef]
149. Anthony, J.W.; Bideaux, R.A.; Bladh, K.W.; Nichols, M.C. (Eds.) *Handbook of Mineralogy 2 (Silica, Silicates)*; Mineralogical Society of America: Chantilly, VA, USA, 1995.